JGR Atmospheres

RESEARCH ARTICLE
10.1029/2020JD033988

Interactions of Large-Scale Dynamics and Madden-Julian Oscillation Propagation in Multi-Model Simulations

Ashley Heath[1], Alex O. Gonzalez[1], Maria Gehne[2], and Alejandro Jaramillo[3]

[1]Department of Geological and Atmospheric Sciences, Iowa State University, Ames, IA, USA, [2]Cooperative Institute for Research in Environmental Sciences, University of Colorado Boulder, and NOAA/Earth System Research Laboratory, Boulder, CO, USA, [3]Centro de Ciencias de la Atmósfera, Universidad Nacional Autónoma de México, Mexico City, Mexico

Key Points:

- A west/east zonal wind speed ratio shows models with a large Rossby wave or small Kelvin wave response to convection have a stagnant Madden-Julian Oscillation (MJO)
- Poor model Rossby and Kelvin waves are associated with anomalous moistening co-located with convection and drying to the east, respectively
- Spectral analyses show deficient MJO, Rossby, and Kelvin wave zonal wind and rainfall in poor models but suggest model-wide coupling biases

Correspondence to:
A. O. Gonzalez,
agon@iastate.edu

Citation:
Heath, A., Gonzalez, A. O., Gehne, M., & Jaramillo, A. (2021). Interactions of large-scale dynamics and Madden-Julian Oscillation propagation in multi-model simulations. *Journal of Geophysical Research: Atmospheres*, *126*, e2020JD033988. https://doi.org/10.1029/2020JD033988

Received 28 SEP 2020
Accepted 6 MAR 2021

Abstract The underrepresentation of the Madden-Julian Oscillation (MJO) in climate models remains a challenge, limiting our ability to improve medium- to extended-range atmospheric prediction. Motivated by recent work identifying the importance of the ratio of equatorial Rossby (ER) to Kelvin wave circulations in MJO propagation, this study examines MJO dynamics in 25 climate model simulations. We find that poor MJO models simulate anomalously large ER wave circulations to the west and small Kelvin and ER wave circulations to the east of the convective center. To quantify the role of circulation asymmetries in MJO propagation, we formulate a new west/east (W/E) zonal wind speed ratio. Our W/E ratio differs from other similar metrics in that it implicitly accounts for the ER wave gyres and it can be applied at all levels. Poor model ER wave biases are associated with excessive 700–1000-hPa convergence, convection, and vertical moisture advection co-located and west of the convective center while Kelvin and ER wave biases to the east are associated with a weaker dry anomaly and smaller horizontal moisture advection at 450–750-hPa. Together, these biases help explain the stationary and slight westward MJO propagation in poor models. Space-time spectral analyses of the zonal wind and precipitation confirm that good models produce realistic power, coherence, and phase for the MJO while poor models vastly underrepresent Kelvin waves and the MJO. Even though Kelvin waves are more realistic in good models, there are still model-wide biases in circulation-convection coupling for ER waves and Kelvin waves.

Plain Language Summary Intraseasonal variability lies between weather and climate time scales and has been shown to extend the traditional two-week weather predictability limit to up to five weeks. The Madden-Julian Oscillation (MJO) is an intraseasonal atmospheric mode that couples tropical atmospheric clouds and circulations. Key features of the MJO include a large region of strong clouds and precipitation surrounded by large regions of dry conditions that together propagate eastward from the Indian Ocean to the Pacific Ocean. The MJO contains eastward winds to the west and westward winds to the east of the strong clouds near the surface and reversed winds in the upper atmosphere. This study investigates the differences of the large-scale circulations associated with the MJO between a set of six good and poor models to explain the fidelity of MJO propagation. We find that poor models tend to have too strong of circulations and clouds in the lower atmosphere co-located with and to the west of the MJO's cloud center, causing stagnant, or even westward, propagation. A space and time investigation into other atmospheric modes of variability demonstrates that all models, especially poor models, have significant biases in the interactions between large-scale circulations and clouds.

1. Introduction

The Madden-Julian Oscillation (MJO) is an intraseasonal (30–90 days time scale) and planetary scale (zonal wavenumber 1–3) tropical disturbance that initiates over the Indian Ocean and propagates eastward at about 5 m s^{-1} (Madden & Julian, 1971, 1972). The MJO influences global climate and weather, including but not limited to tropical cyclone activity, convectively coupled equatorial waves, monsoons and extratropical weather extremes (see review by C. Zhang, 2013). A longstanding issue in the Earth system modeling community is that the MJO is poorly represented in climate models (Ahn et al., 2017; Lin et al., 2006) and weather forecast models (see review by H. Kim et al., 2018). Common model biases include amplitude biases and a lack of eastward propagation (e.g., Hung et al., 2013; Jiang et al., 2015).

Significant progress has been made recently in understanding model MJO biases mainly centered around moist static energy (MSE) as a proxy for tropical convection (Raymond & Fuchs, 2009; Sobel & Maloney, 2013; Yu & Neelin, 1994). Investigations of the column-integrated MSE budget in model simulations have identified horizontal and vertical MSE advection as crucial to the simulation of coherent eastward MJO propagation (e.g., Adames & Wallace, 2015; Jiang, 2017; D. Kim et al., 2014; Maloney, 2009; Sobel et al., 2014; B. Wang & Lee, 2017; L. Wang et al., 2017; L. Wang & Li, 2020a). More specifically, the horizontal and vertical advection of background MSE by the intraseasonal large-scale circulation appear to be the leading processes (Adames & Wallace, 2015; Ahn, Kim, Ham, & Park, 2020; Gonzalez & Jiang, 2017; Hsu & Li, 2012; Jiang, 2017; H. Kim et al., 2018; B. Wang & Lee, 2017; L. Wang & Li, 2020a, and many others). Poor MJO models tend to have dry biases in lower free tropospheric specific humidity as well as anomalously small low-level easterlies surrounding the Maritime Continent (e.g., Ahn, Kim, Ham, & Park, 2020; Gonzalez & Jiang, 2017; Jiang, 2017; Jiang et al., 2015; B. Wang & Lee, 2017). Thus, there is a significant role of the large-scale circulation in the MSE budget and MJO propagation.

While numerous modeling studies have focused on the impact of MSE and moisture on the MJO, there is still debate about the details of how the large-scale circulation impacts the MJO, as emphasized recently by a review article about the current state of MJO dynamical theory (C. Zhang et al., 2020). It has become apparent that there is a spatial asymmetry between the circulations to the west and east of the MJO's convection and the asymmetry is a necessary component to simulate an eastward propagating MJO (L. Wang et al., 2017; B. Wang & Lee, 2017; L. Wang & Li, 2020a). During the active convective MJO phase, there is a coupled equatorial Rossby (ER) wave versus Kelvin wave large-scale circulation structure (Gill, 1980; Matsuno, 1966), with low-level westerly winds to the west and low-level easterlies to the east of the precipitation center with reversed winds in the upper troposphere (Rui & Wang, 1990; C. Zhang, 2005).

There are two theories on how these large-scale circulation asymmetries impact MJO propagation. The first theory postulates that as the ER wave circulation weakens and/or the Kelvin wave circulation strengthens, MJO eastward propagation increases (Chen & Wang, 2020; B. Wang & Chen, 2016; B. Wang et al., 2016; B. Wang & Lee, 2017). This theory is centered around boundary layer moisture convergence moistening the free troposphere and destabilizing the atmosphere to the east of the MJO's convective center, where the Kelvin wave circulation is strongest (Gill, 1980; Matsuno, 1966). Motivated in part by this theory, a new set of MJO metrics centered around horizontal asymmetries of the dynamics associated with the MJO were recently developed as key characteristics to its eastward propagation (B. Wang et al., 2018).

Meanwhile, the second theory poses that as the intensity of both the ER and Kelvin wave circulation responses increase, the MJO propagates eastward faster (L. Wang et al., 2017; L. Wang et al., 2018; L. Wang & Li, 2020a). This theory is centered around changes in the zonal asymmetry of the MSE budget, with larger ER and Kelvin wave responses both contributing to an increase in MSE asymmetry. As the ER wave response increases, the negative MSE tendencies to the west increase; as the Kelvin wave response increases, the positive MSE tendencies to the east increase. L. Wang et al. (2017) showed strong positive correlations between ER wave and Kelvin wave dynamical strengths and either MJO propagation skill or phase speed in the 500- to 800-hPa layer in support of this theory.

In a similar vein as these dynamical theories, there are still open questions as to how the MJO's circulation and convection interact with other convectively coupled modes of variability and how those modes affect the MJO's eastward propagation (Fuchs-Stone et al., 2019; Gonzalez & Jiang, 2019; Guo et al., 2015; Jiang et al., 2015; Kikuchi et al., 2012, 2018). Guo et al. (2015) suggested that models with the best MJO rainfall propagation have higher fractional precipitation variances for all convectively coupled equatorial waves except ER waves. They also suggest the precipitation variance of ER waves has no correlation with model MJO propagation in terms of its fractional or absolute variance. It is still unknown if these conclusions hold for spectral and cross-spectral analyses involving dynamical variables, which are critical for understanding dynamical-convective coupling and ultimately, MJO propagation.

The goal of this study is to build upon the existing framework on the model representation of ER and Kelvin waves and their relative roles in MJO propagation centered around equatorial wave dynamics (Gill, 1980; Matsuno, 1966). We propose a new west/east zonal wind speed ratio, which effectively quantifies both Kelvin waves and ER waves, including their vorticity aspects. Similar to L. Wang et al. (2018), we examine how

the roles of ER and Kelvin waves in MJO propagation change as a function of height. We also build upon Guo et al. (2015) by addressing not only model representation of precipitation and zonal wind among convectively coupled equatorial waves and the MJO but also the coupling of model simulated precipitation and zonal wind variability in cross-spectral analyses.

2. Data Sets

2.1. Observational Data

The observational data sets used in this study were the European Center for Medium-Range Weather Forecasting (ECMWF) ERA-Interim reanalysis (ERA-Interim, Dee et al., 2011) for dynamic and thermodynamic variables and version 3B42 v7 of the Tropical Rainfall Measuring Mission rainfall observations (TRMM, Huffman et al., 2007) for the period 1998–2012. Both ERA-Interim and TRMM data were interpolated daily onto grids that match the global climate model (GCM) output, that is, 2.5° × 2.5° at 22 standard vertical pressure levels.

2.2. Climate Model Data

A global model intercomparison project was launched in 2010 under the Year of Tropical Convection MJO Task Force (MJOTF) and Global Energy and Water Cycle Experiment Atmospheric System Study (GASS) program (Jiang et al., 2015; Petch et al., 2011). This study focused on the 20-year (1991–2010) climate model simulation component of the MJOTF/GASS project and investigated 25 GCM simulations. Details about each model can be found in Table 1. The MJOTF models were either an atmospheric-only GCM (AGCM) or an atmosphere-ocean coupled GCM (CGCM). The AGCM model runs had weekly sea surface temperatures (SSTs) and sea ice concentrations specified as lower boundary conditions based on the National Oceanic and Atmospheric Administration Optimum Interpolation V2 product (Reynolds et al., 2002). Output from all GCMs was interpolated from six-hourly to daily data on standard horizontal 2.5° × 2.5° grids and 22 vertical pressure levels. All of the GCMs are based on a conventional parameterization approach to depict cumulus processes except the coupled SPCCSM3, which used the "superparametrization" technique (Randall et al., 2003). Superparameterization involves integrating a 2-D cloud-resolving model into each atmospheric grid column of the host model as a replacement to the conventional cumulus parameterizations. There are five coupled CGCMs in addition to the SPCCSM3; CanCM4, CNRM_CM, ECHAM5_SIT, ECHAM6, and PNU_CFS while the rest of the models are AGCMs. Three simulations were conducted using the CNRM GCM: CNRM_AM, CNRM_CM, and CNRM_ACM. The CNRM_AM is an AGCM integration forced by the observed weekly SSTs and sea ice. The CNRM_CM is a CGCM run and the CNRM_ACM was an AGCM forced by the monthly mean SST and sea ice output from the coupled run (CNRM_ACM).

Other models in this data set were based on different versions and/or modifications of the NCAR CAM model including the CAM5_ZM (v5), ISUGCM (v3), NCAR CAM5 (v5), UCSD_CAM3 (v3) and TAMU_CAM4 (v4). Notably, the TAMU_CAM4 constrained both the horizontal and vertical distribution of model heating throughout the tropics using the "observed" latent heating structure for the MJO based on TRMM estimates (Lappen & Schumacher, 2012).

3. Methods

Our analyses focus on the MJO during the boreal winter season, from November to April. Anomalies were computed for all variables and have the climatological annual cycle (annual mean plus three leading harmonics) and any linear trend removed. Out of the 25 MJOTF models the six best and worst performing models are grouped together (good and poor models respectively). Model performance is determined based on the MJO propagation skill score defined below. To highlight the inter-model extremes, the good and poor model sets are compared to a random selection among all 25 MJOTF models through a bootstrap analysis. Six models were randomly selected from the set of 25 and averaged and compared to the good and poor model sets. This process was repeated 5,000 times to approximate the distribution of the sample mean and then the 95% confidence bounds for each analyzed variable were determined from the re-sampled distribution. This method is different than what is typically been applied in other MJOTF studies that simply test

Table 1
A List of Participating Models in the 20-Year Climate Simulations

Model name	Institution	Reference
ACCESS1	Centre for Australian Weather and Climate Research, Australia	(Zhu et al., 2013)
BCC_AGCM2.1	Beijing Climate Center, China Meteorological Administration	(Wu et al., 2010)
CCCma_CanCM4	Canadian Centre for Climate Modeling and Analysis, Canada	(Merryfield et al., 2013)
CNRM_ACM	Centre National de la Recherche Scientifique/Météo-France, France	(Voldoire et al., 2013)
CNRM_AM		
CNRM_CM		
CWB_GFS	Central Weather Bureau, Taiwan	(Liou et al., 1997)
EC_GEM	Environment Canada, Canada	(Côté et al., 1998)
IAP_FGOALS_s2	Institute of Atmospheric Physics, Chinese Academy of Sciences, China	(Bao et al., 2013)
ISU_GCM	Iowa State University, United States	(Wu & Deng, 2013)
LLNL_CAM5ZM	Lawrence Livermore National Laboratory, United States	(Song & Zhang, 2011)
MIROC5	Atmosphere and Ocean Research Institute (AORI)/ National Institute for Environmental Studies (NIES)/ JAMSTEC, Japan	(Watanabe et al., 2010)
MPI_ECHAM6	Max Planck Institute for Meteorology, Germany	(Stevens et al., 2013)
MRI_AGCM	Meteorological Research Institute, Japan	(Yukimoto et al., 2012)
NASA_GEOS5	NASA Global Modeling and Assimilation Office, United States	(Molod et al., 2012)
NASA_GISS_E2	NASA Goddard Institute for Space Studies, United States	(Schmidt et al., 2014)
NCAR_CAM5	NCAR Community Atmospheric Model 5	(Neale et al., 2012)
NCAR_SPCCSM	George Mason University, United States	(Stan et al., 2010)
NCEP_CFSv2	NOAA/NCEP Climate Prediction Center, United States	(Saha et al., 2014)
NCHU_ECHAM5_SIT	Academia Sinica, Taiwan	(Tseng et al., 2015)
NRL_NAVGEM1	U.S. Naval Research Laboratory, United States	
PNU_CFS	Pusan National University, South Korea	(Saha et al., 2006)
SMHI_ECEarth3	Rossby Centre, Swedish Meteorological and Hydrological Institute, Sweden	
TAMU_CAM4	Texas A&M University	(Lappen & Schumacher, 2012)
UCSD_CAM3	Scripps Institution of Oceanography, United States	(G. J. Zhang & Mu, 2005)

the null hypothesis that the anomalies are significantly different than zero. The method used here can be thought of as a measure of how extreme the good and poor model groups are compared to a resampling of the model population. It also means that even if there are sizable anomalies that are not statistically significant, those anomalies could indicate common model biases.

3.1. Model MJO Propagation Ranking

In order to rank each MJOTF model's MJO propagation, a precipitation-based intraseasonal index (PII) is produced for each model (S. Wang, 2020). It is constructed from bandpass-filtered (20–100 days) precipitation anomalies projected onto the second empirical orthogonal function (EOF2) of the observed January 15 PII shown in Figure 1 (S. Wang, 2020). EOFs for a particular day of the year are used rather than time averaged EOFs because they retain their orthogonality. This study focuses on the projections of 20–100 days precipitation anomalies onto the EOF2 structure as it is centered over the central Indian Ocean. The same could be done for the EOF1 to understand MJOs that form in the western Indian Ocean, which is left for future studies. The model and observed PIIs are used extensively to perform linear regressions and they are standardized to a 3 mm day^{-1} unfiltered rainfall anomaly averaged over 10°S–10°N and 60°E–100°E (black box in Figure 1) to remove precipitation amplitude dependence. Note that these methods are slightly different than those used in many other MJO studies using the MJOTF models, which devise precipitation-based

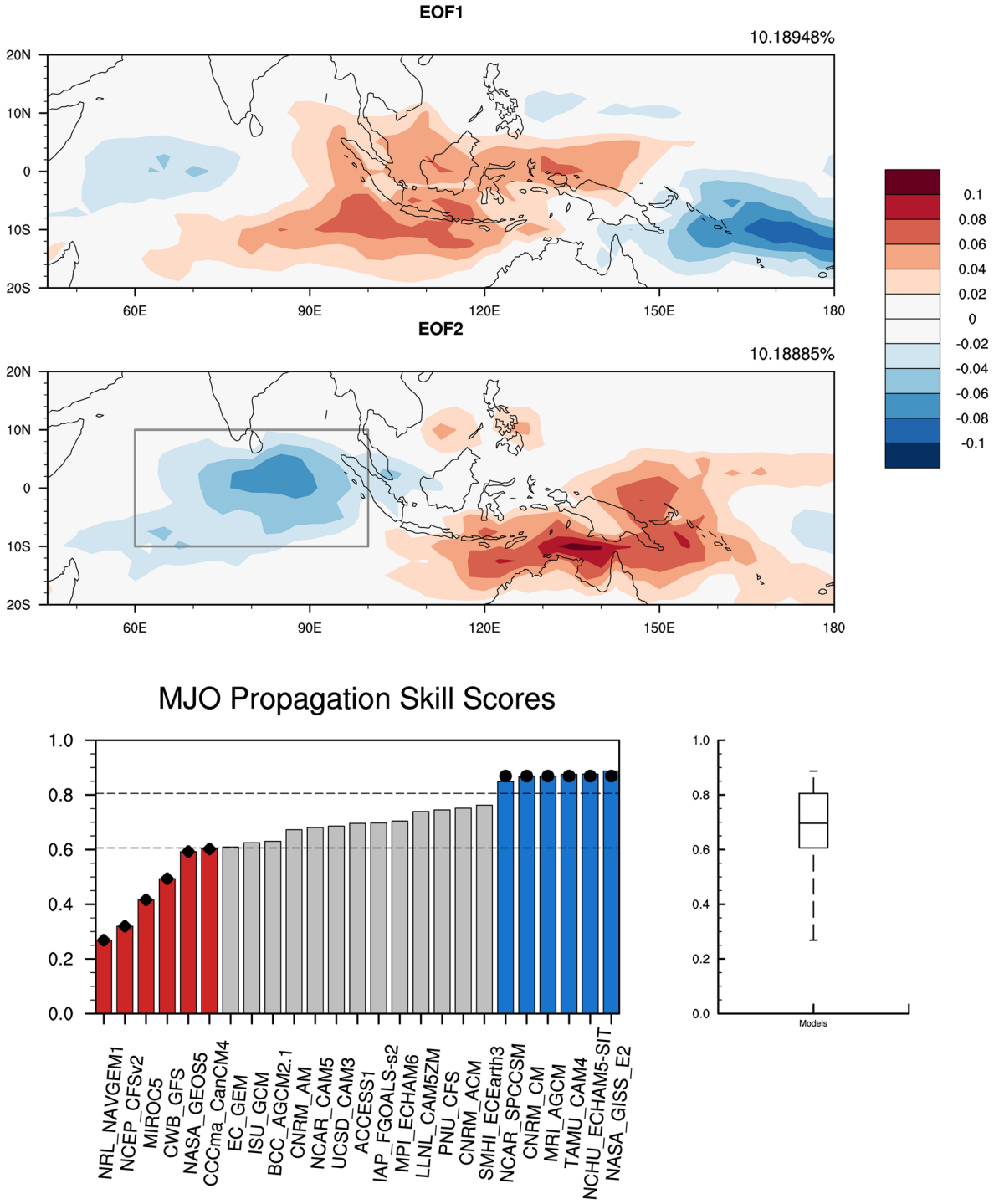

Figure 1. (Top) The first two January 15 empirical orthogonal function (EOF) structures using the precipitation-based Madden-Julian Oscillation (MJO) index (S. Wang, 2020). A projection-based MJO index for each model is formulated based on precipitation projections onto EOF2 over 60°–100°E and 10°S–10°N. The amount of variance explained for each EOF is shown on the top right. (Bottom) The MJO propagation skill scores for each MJO Task Force (MJOTF) model. The good models are blue (circle) and the poor models are red (diamond). The 25th and 75th percentiles of the skill scores are plotted as the dotted lines with the full distribution shown on the right.

intraseasonal indices by simply averaging over set spatial regions rather than projecting onto the observed precipitation spatial distribution.

An alternative method for producing a precipitation-based intraseasonal index is to carry out an EOF analysis on precipitation anomalies for all MJOTF models using the leading principal components (PCs). However, not all models have a coherently propagating MJO and thus, they do not have an EOF pair that is well-separated from the neighboring EOFs. Nonetheless, we perform an EOF analysis following similar methods as S. Wang (2020), with the main distinction being that our EOF analysis is for November through April and it is not a function of day of the year. The EOF analysis is performed on 20–96 days bandpass-filtered precipitation anomalies for 20°S–20°N and all longitudes. Following S. Wang (2020), we retain eastward zonal wavenumbers only, that is, the zonal mean and westward wavenumbers are removed. All MJOTF models have a leading EOF pair that is well separated from EOF three except eight models: NRL_NAVGEM1, MIROC5, CWB_GFS, CCCma_CanCM4, EC_GEM, ISU_GCM, CNRM_AM, and IAP_FGOALS-s2. These results support our decision to use the observed PII EOFs to construct each model's PII rather than model-derived PCs.

A MJO propagation skill score for each GCM was measured by pattern correlations of Hovmöller (time-longitude) diagrams of anomalous rainfall between each MJOTF model and TRMM observations over lags −20 to +20 days and from 50°–180°E. These pattern correlations omit lags −2 to +2 days and 75°–85°E, allowing for a wider range of correlation values (B. Wang & Chen, 2016). The Hovmöller diagrams are unfiltered rainfall anomalies averaged over 10°S–10°N and lag regressed onto each model's PII.

Figure 1 shows all of the MJO propagation skill scores along with the statistical distribution among the 25 models. The top (bottom) six models from this MJO skill score will be used in composite analyses and are considered the good (poor) MJO models for this study. The six good models are CNRM_CM, NASA_GISS_E2, NCAR_SPCCSM, NCHU_ECHAM5_SIT, MRI_AGCM, and TAMU_CAM4 and the six poor models are CCCma_CanCM4, CWB_GFS, MIROC5, NASA_GEOS5, NCEP_CFSv2, and NRL_NAVGEM1. Groups of six models are chosen because they lie outside of the 25th and 75th percentiles of the model MJO propagation skill score distribution.

3.2. Wavenumber-Frequency Spectral Analysis

A zonal wavenumber-frequency spectral analysis for precipitation and zonal wind anomalies is performed for the November–April season to better understand the differences in equatorial waves and the MJO between good and poor MJO models. To identify equatorial wave modes, a red background spectrum was computed from the raw spectrum and removed from the original spectra to leave statistically significant peaks. The background spectrum was calculated by averaging the symmetric and antisymmetric spectra and smoothed using a 1-2-1 filter in frequency and wavenumber. Smoothing is used to attempt to remove periodic signals that may be present in the spectra at particular wavenumbers and frequencies. The number of passes of the 1-2-1 filter was 10 in frequency and from 10 to 40 in wavenumber, 10 at low frequencies and 40 at higher frequencies increasing in two different steps (Wheeler & Kiladis, 1999). The resulting spectra were calculated for successive overlapping 60-day segments for the boreal winter season with a 15-day overlap and tapering of the ends of each segment. These shorter segments allow for four total segments per winter season rather than two with more commonly used 96-day with 30-day overlap segments and they help produce a more accurate representation of higher frequency equatorial waves (Dias & Kiladis, 2014). The temporal windowing provided by the tapering helps minimize effects of spectral leakage and the data loss from tapering is minimized by the overlapping segments. The power for each variable is summed over 15°S–15°N and is averaged over all available segments for the 14 winter seasons in TRMM and ERA-Interim and 19 winter seasons in the MJOTF climate model data sets. A cross-spectral wavenumber-frequency analysis is also performed using the same segments. The cross-spectral analysis yields space-time coherence-squared and phase spectra which can be used to assess the strength of the coupling between precipitation and zonal wind anomalies.

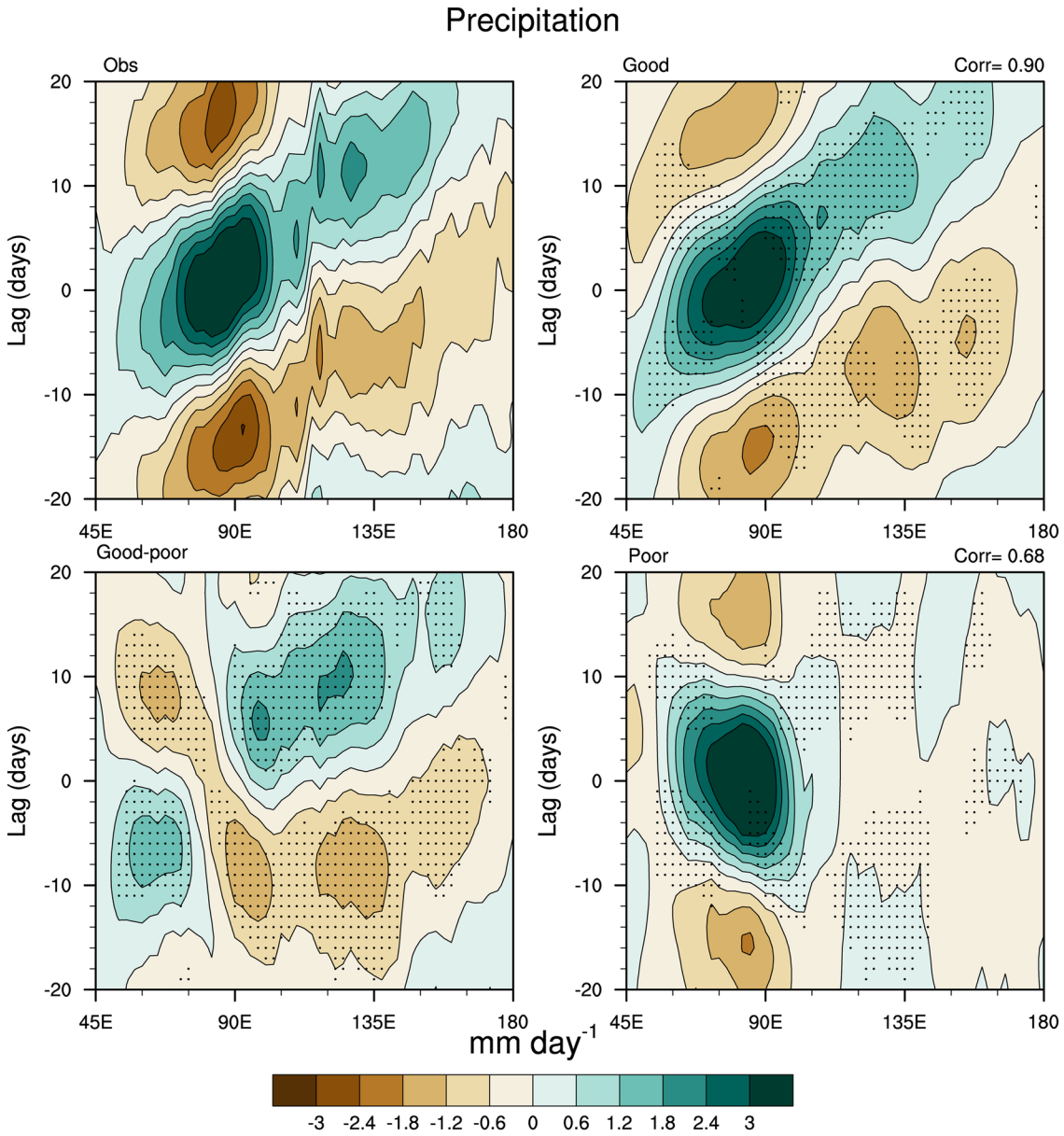

Figure 2. Hovmöller diagrams of 10°S–10°N averaged unfiltered precipitation anomalies for Tropical Rainfall Measuring Mission (TRMM) observations (top left), good models (top right), poor models (bottom right) and good-poor models (bottom left) regressed onto each precipitation-based intraseasonal index (PII). The pattern correlations between TRMM and the respective set of models is shown on the top right. The $\alpha = 5\%$ statistically significant points from bootstrapping using a sample population involving all 25 Madden-Julian Oscillation Task Force (MJOTF) models are plotted in the model plots.

4. Results

4.1. Precipitation Structure

To assess the accuracy of MJO propagation in the MJOTF/GASS models, Figure 2 shows 10°S–10°N averaged unfiltered rainfall anomalies regressed onto each PII for the good and poor model composites and TRMM. As a reminder, the black dots for all spatial plots represent locations where each model composite is statistically significantly different than a random selection of six MJOTF models at the $\alpha = 5\%$ level based on a bootstrapped distribution involving all 25 MJOTF models. The good models accurately capture the eastward propagation of the MJO throughout the entire Indo-Pacific domain. However, the poor models have a stationary and even slight westward propagation over the Indian Ocean. The stark differences shown here in propagation direction between the good and poor models are similar to what has been shown by

previous studies using the MJOTF models (e.g., Jiang, 2017; Jiang et al., 2015; L. Wang et al., 2017; B. Wang et al., 2018).

The large-scale distribution of precipitation is a defining factor of the MJO. Therefore, the differences in precipitation anomalies between the two model sets and TRMM data are explored in Figure 3. Regression of unfiltered precipitation anomalies onto the PII time series shows a similar pattern of zonally elongated positive precipitation over the Indian Ocean between the good model set and the TRMM data, which is supported by its high pattern correlation of 0.87. However, despite each model's PII involving projections onto the observed PII EOF2 structure, poor models have a bulls-eye like pattern rather than a zonally elongated pattern of the positive precipitation anomalies over the Indian Ocean. In particular, the good-poor plot shows the good models have significantly more precipitation in the southwest Indian Ocean and near the western Maritime Continent in addition to having less precipitation south of India. The good-poor panel also suggests that the good models have stronger dry anomalies north and south of the Maritime Continent and over the Pacific Ocean. These differences in precipitation structure will become important as we will relate them to the differences in diabatic heating structures in Section 4.4.

4.2. Zonal Wind Structure

To inform us about the potential interactions between MJO dynamics and precipitation, Figure 4 shows the unfiltered 850-hPa zonal wind anomalies regressed onto each PII. Note that meridional wind anomalies showed minimal statistically significant points, implying the good and poor model sets do not stand out when compared to the rest of models. Instead, we will infer the importance of the differences in meridional winds through analyzing how the zonal winds change with latitude, especially west of the convective envelope where ER waves are most prominent in response to a diabatic heat source. Figure 4 shows a broad pattern of westerlies to the west and easterlies to the east of the convection center for the observations and both model sets. Also, there are easterlies poleward of the westerlies wrapping around the large cyclonic gyres typically associated with ER waves. Both model composites have stronger wind speeds than ERA-Interim, especially the good models with larger winds east and west of the convective center. Notably, the westerlies and easterlies to the west are weaker than the easterlies to the east in the ERA-Interim data and the good models, however, the reverse occurs in the poor models. This suggests that the ER waves to the west and the Kelvin waves to the east of the convective center are weaker and stronger, respectively, in the good models. In addition, due to the off-equatorial nature of the stronger easterlies and dry anomaly to the east in good models, there likely is a stronger ER wave response to the dry anomaly (L. Wang et al., 2017). These large-scale differences in low-level zonal wind asymmetries have been previously linked to the relative strength of ER to Kelvin waves and are often thought of as a main predictor of MJO propagation in GCMs (L. Wang et al., 2017; B. Wang & Lee, 2017; B. Wang et al., 2018; L. Wang et al., 2018).

To investigate these basic horizontal zonal wind asymmetries in more detail, Figure 5 shows a 10°S–10°N averaged longitude versus pressure plot of the unfiltered zonal wind anomalies regressed onto each PII. There is a westward tilt with height of the zonal winds anomalies in the ERA-Interim data that has been well documented (e.g., Jiang et al., 2015; Kiladis et al., 2005). The good model composite reproduces this westward tilt with stronger wind speeds among all the plots and much stronger easterly winds than the poor models, especially in the upper levels. The zonal winds are more confined in longitude to the west in the poor models and their low-level westerlies exhibit a slight eastward tilt with height.

As seen in Figure 5, the zonal wind amplitude east and west of the convective center varies greatly with height among the ERA-Interim and both model composites, with ERA-Interim and the good models showing larger easterlies than westerlies throughout the column and an increase in zonal wind speed with height. In contrast, the poor models have similar easterly and westerly wind magnitudes and minimal increase of wind speed with height. These results are suggestive of an important role of an ER wave over Kelvin wave zonal wind ratio at low levels (e.g., B. Wang & Lee, 2017; L. Wang et al., 2018) and zonal wind amplitude at upper levels.

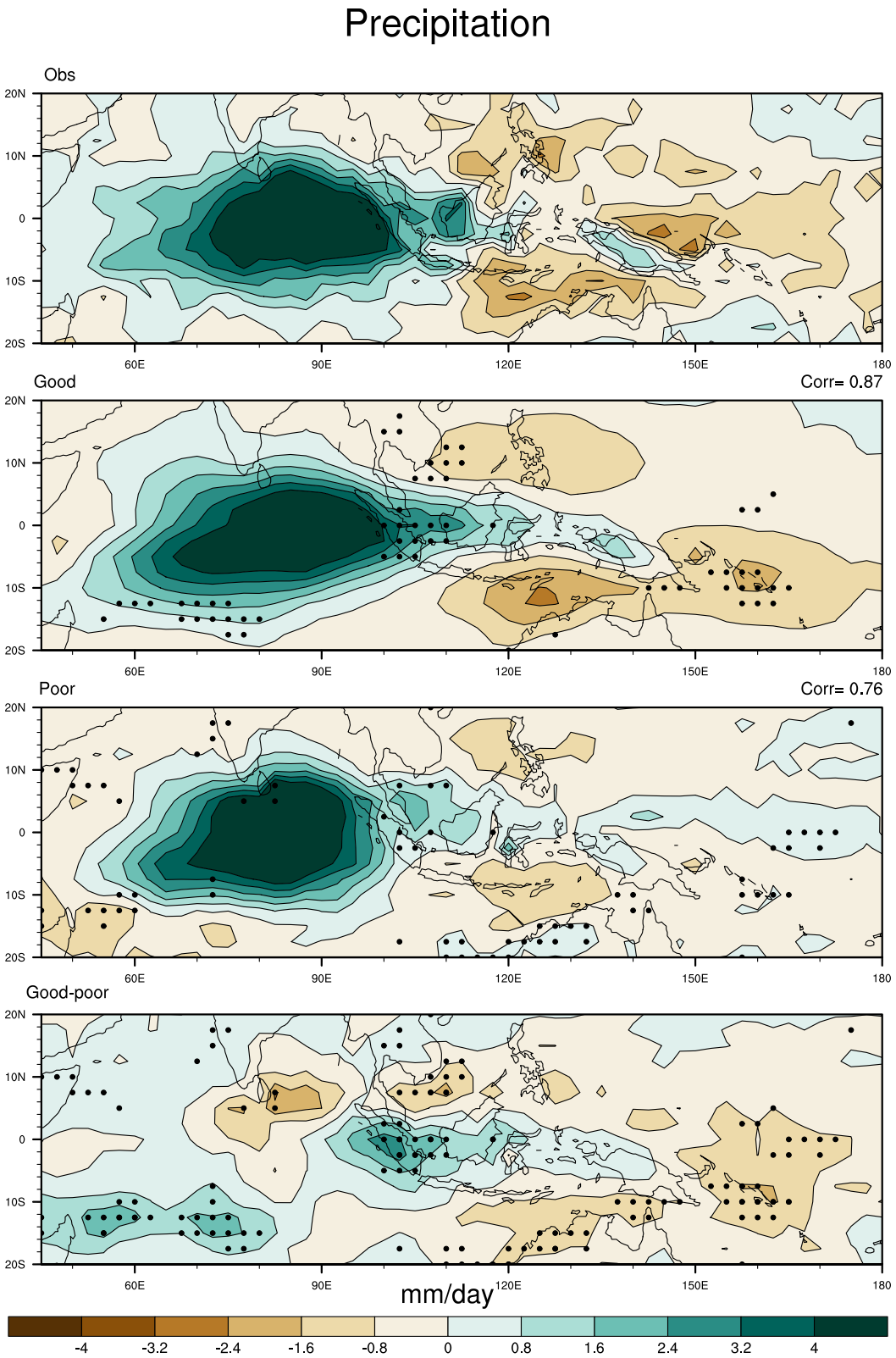

Figure 3. Unfiltered precipitation anomalies regressed onto each precipitation-based intraseasonal index (PII) for Tropical Rainfall Measuring Mission (TRMM), good models, poor models and good-poor models. The pattern correlation between each model group and TRMM is shown on the top right of each plot. The $\alpha = 5\%$ statistically significant points from bootstrapping using a sample population involving all 25 Madden-Julian Oscillation Task Force (MJOTF) models are plotted in the bottom three panels.

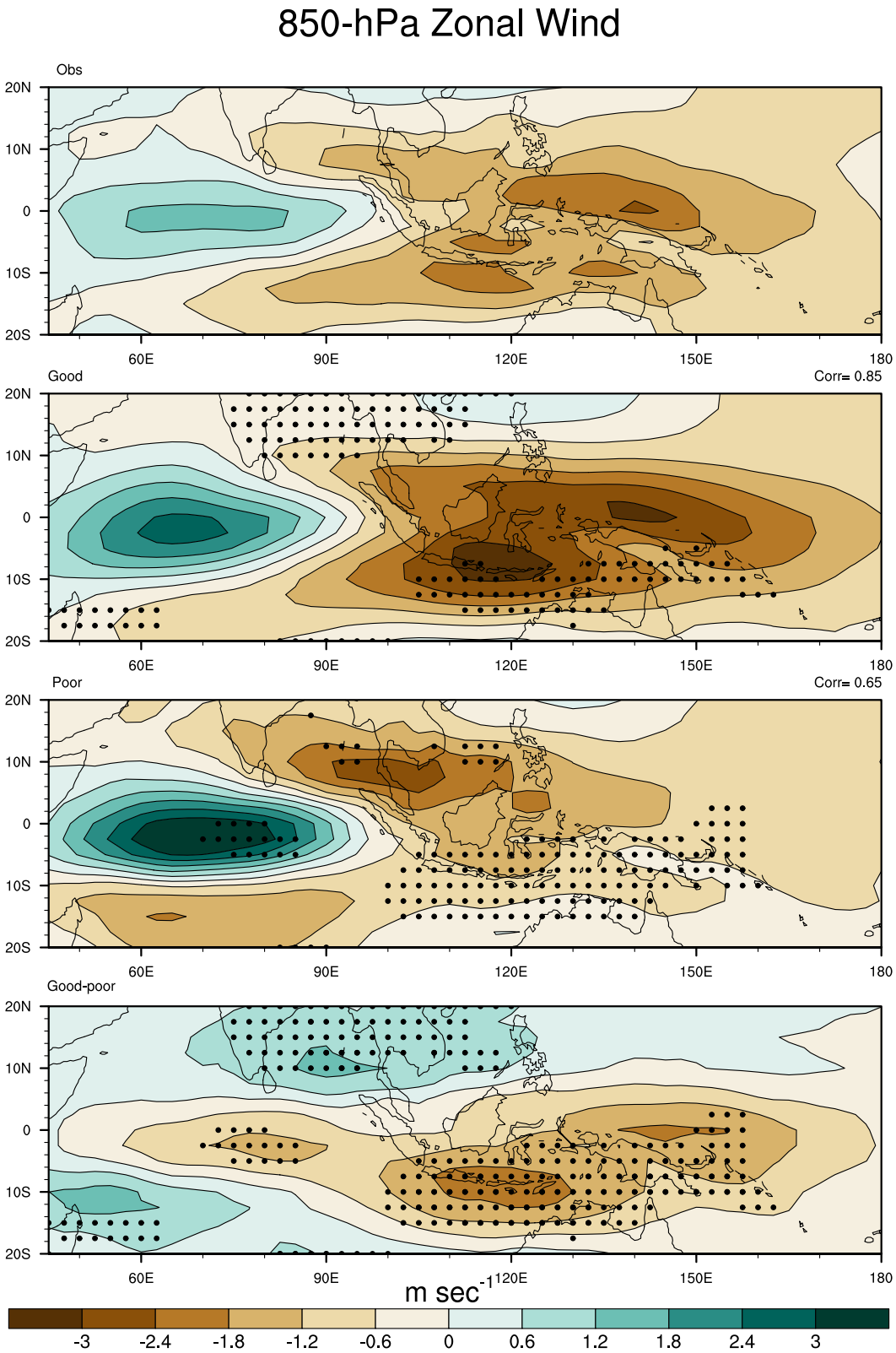

Figure 4. The same as Figure 3 but for unfiltered 850-hPa zonal wind anomalies regressed onto each precipitation-based intraseasonal index (PII) for ERA-Interim, good models, poor models and good-poor models.

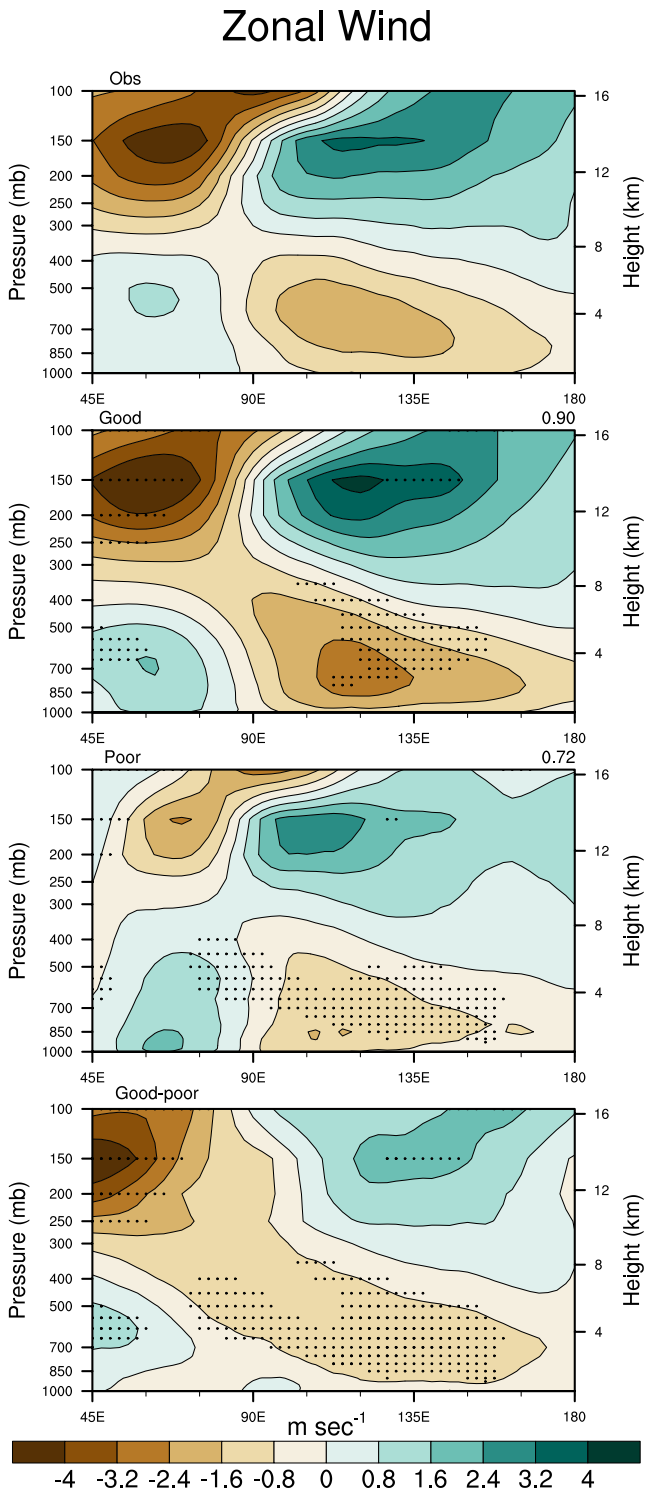

Figure 5. Unfiltered 10°S–10°N averaged zonal wind anomalies regressed onto each precipitation-based intraseasonal index (PII) for ERA-Interim, good models, poor models, and good-poor models. The pattern correlations between ERA-Interim and the respective set of models is shown on the top right. The $\alpha = 5\%$ statistically significant points from bootstrapping using a sample population involving all 25 Madden-Julian Oscillation Task Force (MJOTF) models are plotted in the bottom three panels.

4.3. A West/East Zonal Wind Speed Ratio

To further investigate how these dynamical asymmetries are related to MJO propagation, we devise a new west to east (W/E) zonal wind speed ratio for all pressure levels in ERA-Interim and the MJOTF models. The W/E ratio is computed at each pressure level as the average zonal wind speed in the west part divided by the average zonal wind speed in the east part of the 15°S–15°N, 45°–180°E domain. The W/E ratio can be thought of as an ER/Kelvin wave ratio since ER waves lie to the west and Kelvin waves to the east of a diabatic heat source (Gill, 1980; Matsuno, 1966). However, one must not ignore the possible contribution of the ER wave zonal wind response to the dry anomaly in the eastern part of the domain. Luckily for the MJOTF models, it appears that the ER and Kelvin wave dynamical biases to the east are of the same sign (L. Wang et al., 2017; L. Wang et al., 2018). Note that the ER wave gyre intensity has implicitly been taken into account when the zonal wind speed is used in the W/E ratio, with a strong ER wave response associated with strong westerlies and easterlies in the west part of the domain. The separation between the west and east part of the domain is determined by a critical longitude that varies by data set and pressure level. The critical longitude is defined as the easternmost longitude of ER wave westerlies (low levels) or easterlies (upper levels).

The W/E ratio formulated here is quite similar to what has been used in recent studies to understand how the ratio of ER and Kelvin wave dynamical amplitudes impact MJO propagation (e.g., B. Wang et al., 2018; L. Wang et al., 2018). Three main distinctions exist here: (1) this W/E ratio is not computed over fixed regions west and east of the MJO convection but rather allows flexibility to what longitude and latitude separates the ER and Kelvin wave responses, (2) this W/E ratio takes the vorticity associated with the zonal winds into account as it averages all zonal wind speeds on both sides of the domain, and (3) this W/E ratio can be computed at upper levels. Lastly, similar to L. Wang et al. (2018) but in contrast with B. Wang et al. (2018), our W/E ratio does not use the maximum westerly and easterly wind speeds but rather averages the zonal winds over a wide area, which accounts for each model's large-scale dynamical response.

Correlations between the MJO propagation skill and W/E ratios are shown in Figure 6 (left plot, black line with circles). Very strong anti-correlations of the W/E ratio with MJO propagation skill can be seen in Figure 6 with correlation magnitudes above 0.7 below 450-hPa and a general decrease with height. This implies that models with a larger MJO propagation skill also have a smaller magnitude of the W/E ratio at low levels, indicating stronger Kelvin and ER waves to the east and/or weaker ER waves to the west. The relationship between W/E ratio and MJO propagation skill for each model at 850-hPa is shown in the scatter plot of Figure 6 (right plot). The correlation coefficient at the 850-hPa level is −0.86, indicating that the W/E wind ratio is a metric that can effectively discriminate how accurately the models capture MJO propagation. The individual W/E ratio scatter plot along with Figures 4 and 5 imply that the low-level westerlies equatorward of easterlies to the west are larger than the low-level easterly winds to the east for the poor models while the opposite is true for the good models and ERA-Interim. The wide

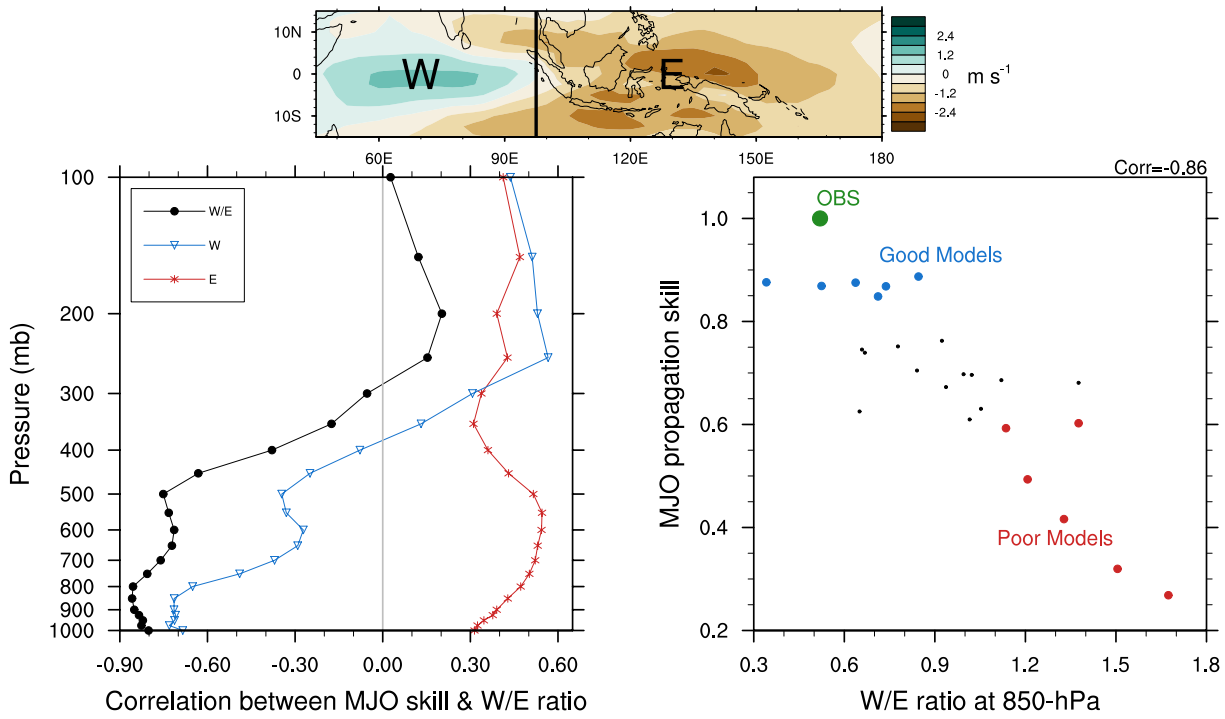

Figure 6. (Left) The correlations between Madden-Julian Oscillation (MJO) propagation skill score and west/east (W/E, black circle line) zonal wind speed ratio and the individual correlations of the west (W, blue triangle line) and east (E, red asterisk line) zonal wind amplitude and MJO propagation skill score for all pressure levels. (Right) A scatter plot example of the MJO propagation skill score and 850-hPa W/E ratio with correlation coefficient in the top right. (Top) The unfiltered 850-hPa zonal wind anomalies used for computing the ERA-Interim W/E ratio including the critical longitude (thick black line) that separates the west and east parts of the domain.

separation of W/E ratio at 850-hPa between the good and the poor model sets further enhance confidence that the two sets have distinctly different large-scale dynamics.

Also shown in Figure 6 are the correlations between MJO propagation skill and the west zonal wind amplitude (W, blue triangles) and the east zonal wind amplitude (E, red asterisks). These calculations provide insight into the individual role of the ER and Kelvin wave wind responses at the different pressure levels and how they affect the W/E ratio. The largest west zonal wind amplitude correlations (≈−0.70) are in the lower levels below 750-hPa where east zonal wind amplitude correlations are substantially smaller; they indicate that the better the models are at representing the eastward propagation of the MJO, the weaker the low-level ER wave wind response is to the west. There are also strong positive west zonal wind amplitude correlations (≈0.55) in the 150–250-hPa layer, indicating that the stronger the ER wave anticyclonic gyres are to the west at upper levels, the larger the MJO propagation skill. This is in agreement with Figure 5, which illustrated excessive westerlies at low-levels and deficient easterlies at upper levels for poor MJO models.

For the east zonal wind amplitude, only positive correlations exist with MJO propagation skill. This indicates that the better the models are at representing the MJO's eastward propagation, the stronger the Kelvin and/or ER wave responses are to the east. The largest correlations of ≈0.5 are located in the 500–750-hPa layer. Near 650-hPa, where the east zonal wind amplitude correlations are relatively large and west zonal wind amplitude correlations are near zero, the correlation implies the Kelvin wave and/or ER wave easterly wind responses to the east are more impactful than the ER wave westerly response to the west to the propagation of the MJO. Near 150-hPa, stronger westerlies to the east are positively correlated with MJO propagation skill. However, the W/E ratio does not show much of a correlation with MJO propagation skill at upper levels because the west and east zonal wind amplitudes have similar correlations with MJO propagation skill.

To summarize, we find that the W/E ratio below 400 hPa is a key metric for MJO propagation, with the ER and Kelvin wave wind response being most critical in the 1000–800-hPa and 750–450-hPa layers, respectively. In addition, the ER and Kelvin wave wind amplitudes are both important in the 150–250-hPa layer for

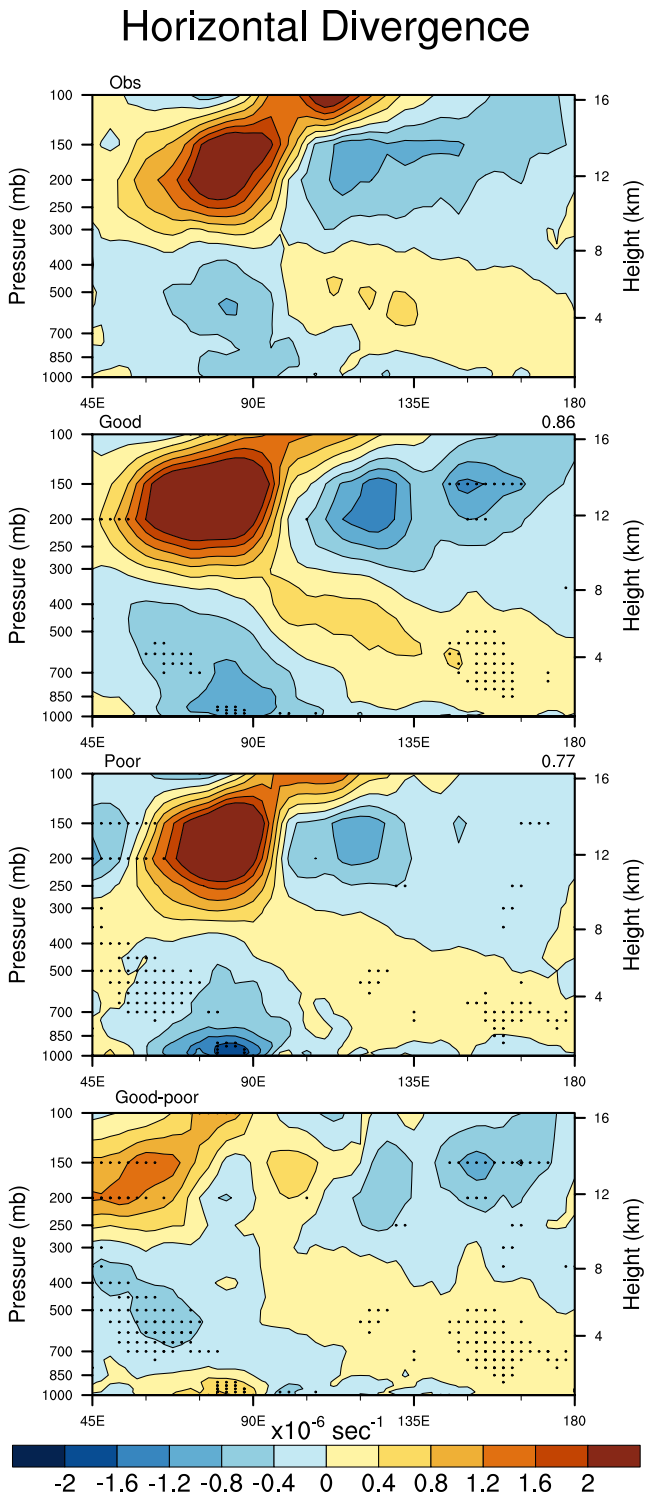

Figure 7. As in Figure 5, but for divergence anomalies.

MJO propagation fidelity but not the W/E ratio. To relate the basic horizontal zonal wind asymmetries to convective characteristics of the MJO, and ultimately, MJO propagation, the vertical structure of divergence, diabatic heating, and moisture advection are explored in the next section.

4.4. Connecting the W/E Ratio to MJO Propagation

4.4.1. Divergence

The large-scale distribution of divergence over the Indo-Pacific region is important to the coupling between MJO dynamics and convection and can help us further interpret the effect of the horizontal wind asymmetry errors in poor MJO models. Figure 7 displays 10°S–10°N averaged longitude versus pressure unfiltered divergence regressed onto each PII. Figure 7 illustrates a westward tilt of divergence and convergence with height which is simulated well in the good models and somewhat present in the poor models. In particular, the poor models have convergence that is constrained to near the surface over the central Indian Ocean with minimal convergence at mid-levels, especially in the western Indian Ocean. The excessive Indian Ocean near surface convergence in the poor models is attributed to both the zonal and meridional components associated with their anomalously strong ER wave response, including excessive equatorward (not shown) and westerly converging winds (e.g., Figures 4 and 5). Note that even though the good models have less Indian Ocean surface convergence than the poor models, both sets of models overestimate low-level convergence. In addition, there is an anomalous mid-level convergence and upper-level divergence couplet in the western Indian Ocean in the good-poor plot suggesting rising motions are too weak on the MJO's back side in the poor models, which may be related to their underrepresentation of statiform heating (B. Wang & Lee, 2017; L. Wang & Li, 2020a). There is also an anomalous mid-level divergence and upper-level convergence couplet over the Pacific Ocean in the good-poor plot which suggests the sinking motion associated with the dry anomaly ahead of the convectively active region is also too weak in poor models.

4.4.2. Apparent Heating

The differences in the zonal cross section of divergence suggest that the poor model convective envelope is too narrow zonally at mid to upper levels on the MJO's back side, it has too much shallow convection, and the dry anomaly ahead of the MJO is too weak. To investigate these ideas further, large-scale characteristics of apparent heating, Q_1/c_p (where c_p is the dry specific heat capacity at constant pressure, Yanai et al., 1973) were evaluated through the center finite difference methods of Hagos et al. (2010), using the equation:

$$\frac{Q_1}{c_p} = \frac{T}{\theta}\left(\frac{\partial \theta}{\partial t} + \mathbf{V}\cdot\nabla\theta + \frac{\omega}{p}\frac{\partial \theta}{\partial \ln p}\right), \quad (1)$$

where T, θ, $\mathbf{V}$, and ω, are air temperature, potential temperature, horizontal velocity, and vertical pressure velocity, respectively.

The 10°S–10°N averaged longitude versus pressure distribution of the unfiltered apparent heating anomalies regressed onto each PII is shown in Figure 8. In ERA-Interim and the good models, there is one mid-level maximum in apparent heating over the central Indian Ocean associated with deep MJO convection as well as a slight westward tilt with height below 200-hPa. On the other hand, the poor models Q_1/c_p positive

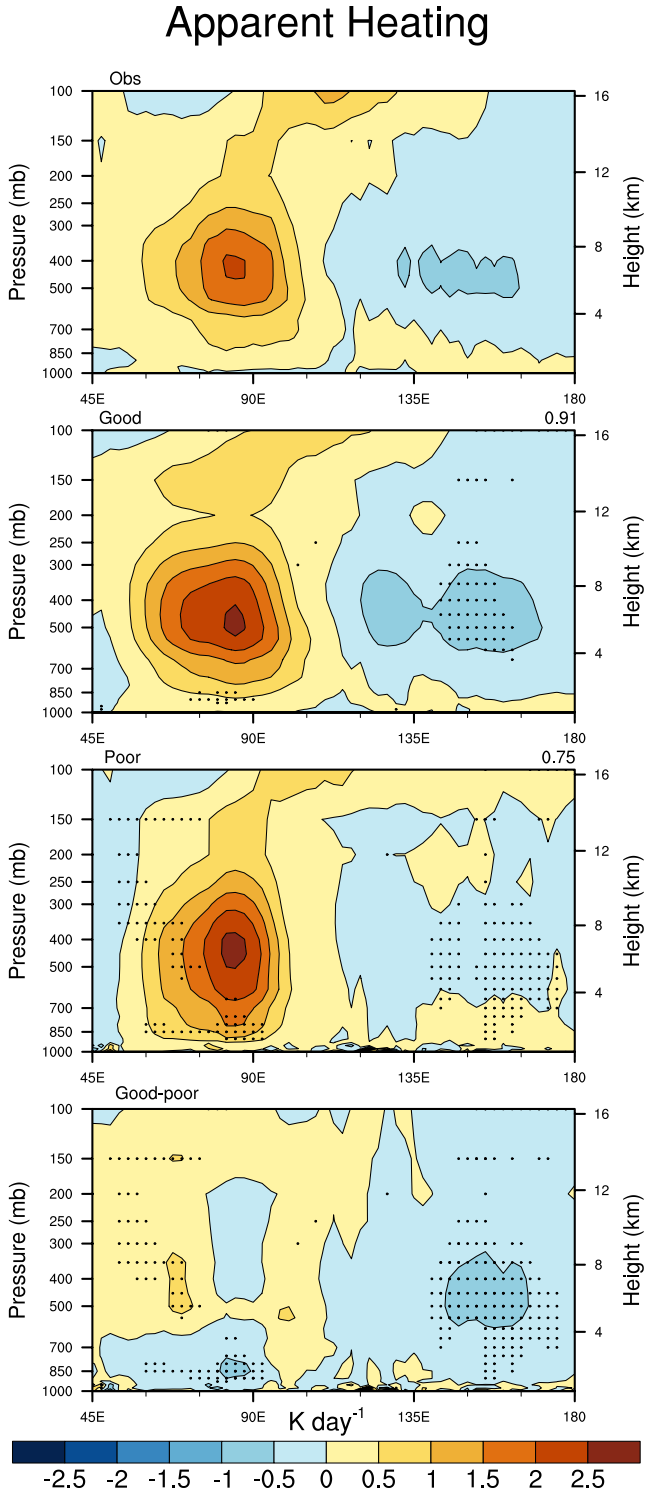

Figure 8. As in Figure 5, but for Q_1/c_p anomalies.

maximum centered over the Indian Ocean does not show as clear of a westward tilt with height below 200-hPa, especially west of 95°E. There is too much heating below 700-hPa and too little heating from 500–150-hPa on the MJO's back side. These results, in agreement with divergence biases in the same areas, imply that the poor models produce too much shallow convection and not enough stratiform convection over the Indian Ocean (e.g., B. Wang & Lee, 2017). Additionally, the Q_1/c_p maximum is wider by 15°–20° in longitude for the good models, which is highlighted by statistically significant differences at 250–500-hPa mainly to the west of the convective center in the good-poor plot. Lastly, the Pacific Ocean area of apparent cooling around 500-hPa is prominent in both ERA-Interim and the good models while nearly absent in the poor models, in agreement with the weaker divergence and convergence couplet in Figure 7. Note the NCEP-CFSv2 model was replaced by EC-GEM in the poor model Q_1/c_p calculation because it had an unrealistic dominant response at 300-hPa.

4.4.3. Horizontal and Vertical Moisture Advection

In this subsection, we connect the biases in zonal winds, divergence, and diabatic heating seen in the poor models to biases in horizontal and vertical moisture advection. The moisture equation used to calculate the moisture advection is given by

$$\frac{\partial q}{\partial t} = -\mathbf{V}\cdot\nabla q - \frac{\omega}{p}\frac{\partial q}{\partial \ln p} - \frac{Q_2}{L_v}, \tag{2}$$

where q is the specific humidity and L_v is the latent heat of vaporization.

Although not shown here, the 10°S–10°N averaged longitude versus pressure distribution of the unfiltered specific humidity anomalies regressed onto each PII show column drying to the west and moistening to the east of MJO convection in ERA-Interim and the good models. For the poor models, there is column moistening co-located and to the west of the convective center and low-level moistening and mid- to upper-level drying to the east of the convective center. Unsurprisingly, these broad structures agree well with the observed and modeled MJO propagation.

Figure 9 shows the 10°S–10°N averaged horizontal advection of specific humidity regressed onto each PII. The poor models do not moisten the column to the east nearly as much as the good models, especially in the 400 to 850-hPa layer over the eastern Maritime Continent and Pacific Ocean. These biases can be directly related to biases in the horizontal advection of the background specific humidity by the anomalous circulation (not shown, see Jiang, 2017; L. Wang et al., 2017). In the eastern region, the poor models have smaller background horizontal moisture gradients and weaker Kelvin wave and ER wave dynamics, including anomalously weak easterly and poleward flow, respectively (Jiang, 2017; L. Wang et al., 2017). The poor models also shown a dearth of drying to the far west of the domain from 400 to 800-hPa (common to many other MJOTF models) despite having a stronger ER wave circulation response than the good models. This appears to have more to do with biases in background horizontal specific humidity gradients than the anomalous circulation (not shown). Based on the horizontal moisture advection tendencies alone, both the good and the poor models should have eastward MJO propagation. Therefore, there must be another process that leads to the stagnant behavior of the MJO in the poor models.

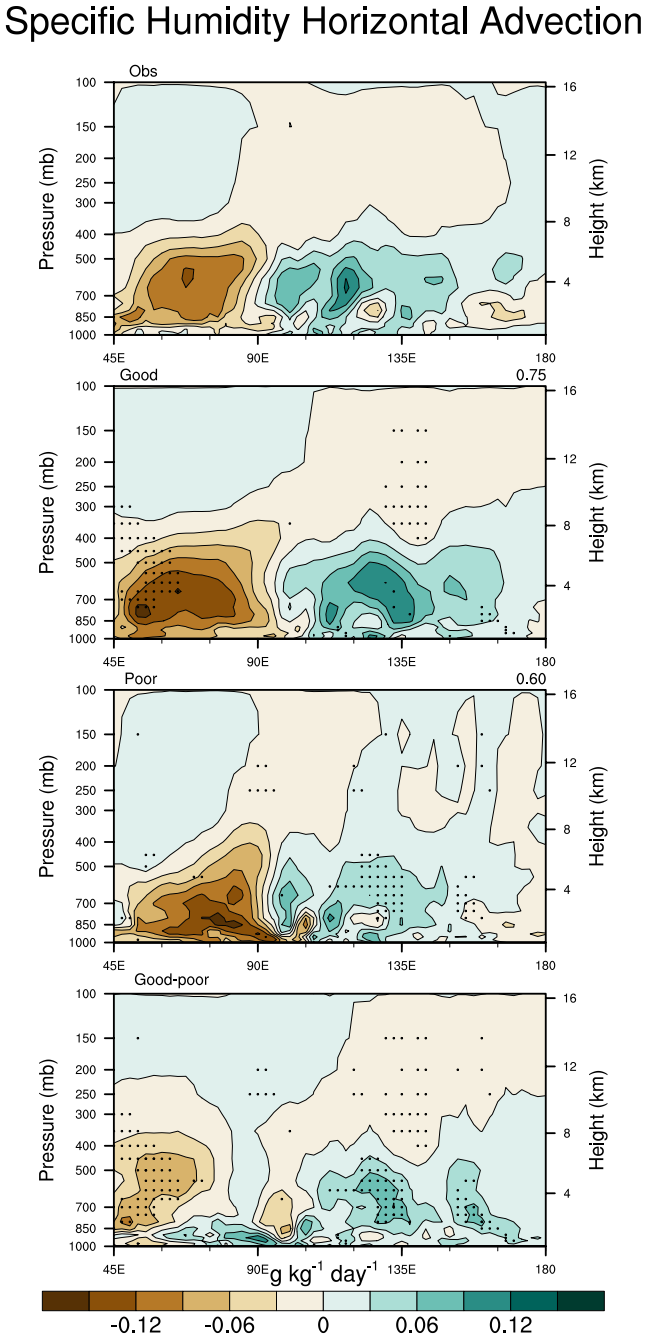

Figure 9. As in Figure 5, but for the specific humidity tendency anomalies due to horizontal advection, $-\mathbf{V} \cdot \nabla q$.

Figure 10 shows the 10°S–10°N averaged vertical advection of specific humidity regressed onto each PII. Based on ERA-Interim and the good models, vertical moisture advection moistens to the east at low levels and to the west at upper levels while being co-located with the MJO precipitation at mid-levels, with a general westward tilt with height. Similar to the cross section of apparent heating, vertical advection is too upright and lacks a westward tilt with height in the poor models. They also lack moistening at the MJO's back side, which even though it does not contribute to the poor models' anomalous moistening to the west, it is directly related to an anomalously large positive MSE tendency to the west (L. Wang et al., 2017; L. Wang & Li, 2020a). The poor models also moisten significantly more to the west than the east in and just above the boundary layer (≈700–1000-hPa). We attribute these biases to the poor models' erroneously large ER wave wind response at low-levels to the west, which is associated with too much boundary layer convergence and shallow convection. If this is the case, the biased ER wave response preconditions subsequent convection to develop right below and to the west of the main convective envelope. Additionally, the poor models lack sufficient mid- to upper-level drying via sinking motion over the Pacific Ocean, which may contribute to their weaker Kelvin and ER wave responses to the east and smaller horizontal moisture advection.

4.5. Spectral Analysis

So far, it has been identified that poor MJO models have significant differences in their large-scale dynamics compared to good models and ERA-Interim which appear to be related to their biased divergence, diabatic heating structures, and moisture budget. In all of our analyses, it has yet to be determined if any modes of variability other than the MJO (e.g., equatorial waves) contribute substantially to these differences as suggested in previous studies (Guo et al., 2015; Kikuchi et al., 2018). A wavenumber-frequency analysis has been used to identify preferred time and space scales of zonally propagating waves for only November through April. Precipitation and zonal wind anomalies were subjected to the spectral analysis along with a wavenumber-frequency cross-spectrum analysis of the two variables. Note that statistical significance is shown in each figure to highlight inter-model extremes and because the spectra and cross-spectra are positive-only fields, the boostrapping method has one tail rather than two.

4.5.1. Wavenumber-Frequency Spectra

Figure 11 shows the individual raw power spectra divided by the background power of precipitation for the symmetric Kelvin, $n = 1$ ER, and $n = 1$ inertia gravity (IG) waves and antisymmetric mixed Rossby-gravity (MRG) and $n = 0$ eastward inertia gravity (EIG) waves. Overlaid in the dotted, dashed, and solid gray curves are $U = -3$, 0, and 3 m s^{-1} Doppler-shifted dispersion curves at 25 meter equivalent depth (Matsuno, 1966). The most prominent signals in the TRMM symmetric spectrum are the MJO at zonal wavenumbers 1–6 and frequencies below 0.06 cycles per day (cpd) and Kelvin waves at zonal wavenumbers 3–10 and frequencies 0.15–0.25 cpd, with ER waves and $n = 1$ IG waves being weaker. The good models have strong powers for ER waves and the MJO with weak to moderate Kelvin waves and weak $n = 1$ IG waves. On the contrary, the poor models have a vastly different symmetric spectrum for precipitation. The strongest signals are below 0.04 cpd and between wavenumbers −10 and +10 near observed ER and MJO signals. There is very minimal asymmetry between westward and eastward wavenumbers, with weaker MJO and slightly stronger ER wave signals and a more

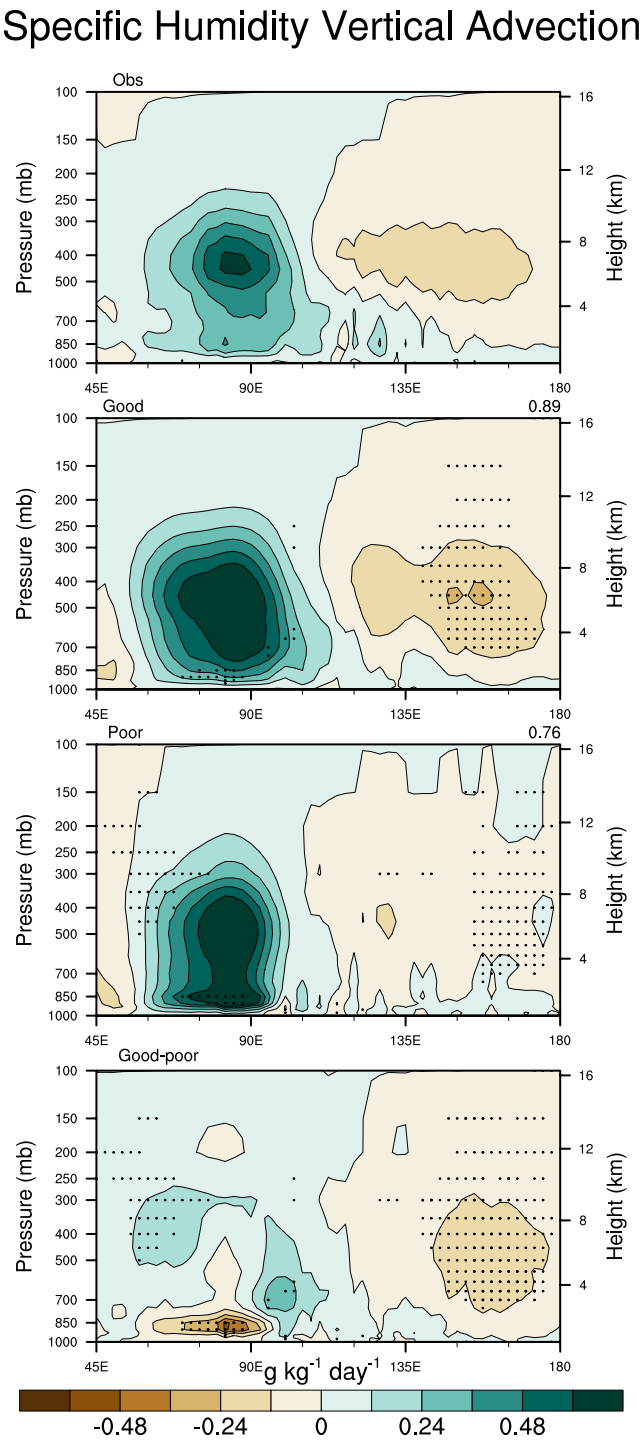

Figure 10. As in Figure 5, but for the specific humidity tendency anomalies due to vertical advection, $-(\omega/p)(\partial q/\partial \ln p)$.

elongated structure in wavenumber compared to the good models, similar to the spectra shown in Jiang et al. (2015). These features may be a sign of standing oscillations in both MJO and ER wave precipitation anomalies for the poor models. In fact, because there are not that many statistically significant points in the poor models at the lowest frequencies, it implies that there are many other MJOTF models with these biased spectral characteristics. Both good and poor models underestimate Kelvin wave precipitation variability, especially poor models, and overproduce ER wave precipitation variability, especially at low frequencies. In addition, the poor models vastly underrepresent the MJO.

For the antisymmetric precipitation spectra, the good and poor models show no significant power for MRG and $n = 0$ EIG waves whereas there are weak to moderate signals in TRMM. In addition, it appears that the poor models have too much power at low frequencies and low eastward wavenumbers while the good models have a similar amount of power compared to TRMM.

Motivated by the the strong relationship of the W/E ratio at low levels with MJO propagation skill in Figure 6, Figure 12 displays the symmetric power spectrum divided by the background for averaged 850 to 1000-hPa zonal winds. ERA-Interim has strong symmetric signals of ER waves, Kelvin waves, the MJO, and external Rossby-Haurwitz waves (eastward wavenumbers 1–4, 0.15–0.30 cpd) with moderate $n = 1$ IG waves. The zonal wind symmetric spectra in the good models is quite similar to that of ERA-Interim for the MJO. However, the good models have relatively weak ER waves, Kelvin waves, and $n = 1$ IG waves and relatively strong external Rossby-Haurwitz waves compared to ERA-Interim. The poor models show even larger discrepancies, with substantially weaker Kelvin and $n = 1$ IG waves, and the MJO. The ER wave zonal wind power in good and poor models is similar and neither peak signal stands out in statistical significance, suggesting model-wide ER wave biases. The ER wave signals peak at the lowest frequencies and are spread out in longitude in the good and poor models which may suggest standing oscillations in zonal winds, similar to what was observed in the poor model precipitation spectra. However, the ER wave power peaks at the lowest frequencies in ERA-Interim too, albeit with much more concentration at wavenumber −3. There is also a distinct separation of the MJO and ER waves at wavenumbers −1 in ERA-Interim and the good models whereas the poor models connect the two together. Similar to the precipitation spectra, the Kelvin waves are too weak in both models sets, especially the poor models.

Due to the insignificant signals in the antisymmetric part of the zonal wind spectra for ERA-Interim and both model sets, these plots are omitted.

Figures 11 and 12 show for the wavenumber-frequency domain, there are specific regions of significant spectral peaks in precipitation and low-level zonal winds. The wavenumber-frequency cross-spectra (coherence-squared and phase) between the precipitation and 850 to 1000-hPa averaged zonal winds were computed to explore whether there is robust coupling between the convection and the dynamics for symmetric and antisymmetric components in Figure 13. For the good and poor models, the phase vectors are shown where the coherence-squared is statistically significant based on our bootstrap approach whereby 5,000 random sets of six MJOTF models

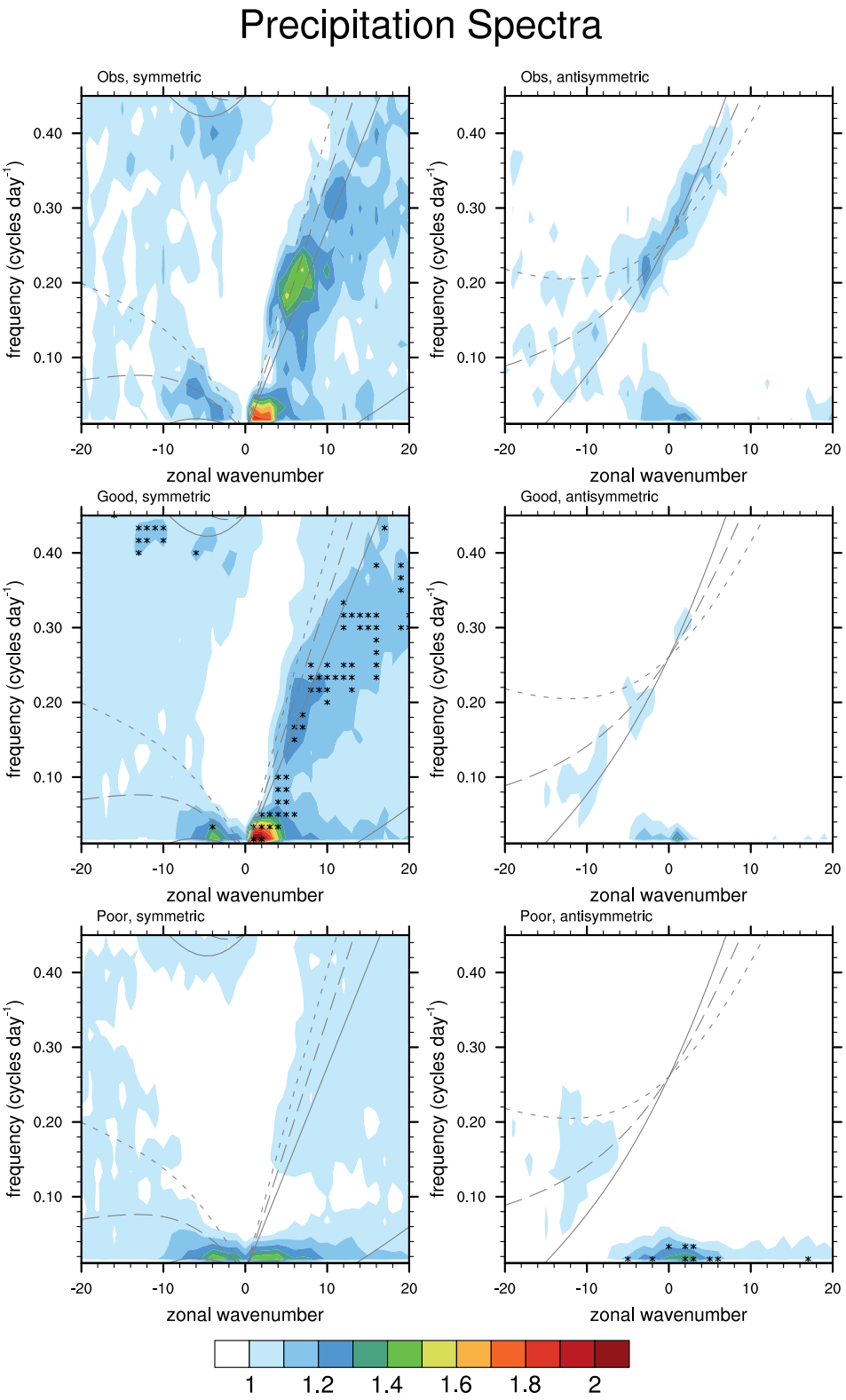

Figure 11. Symmetric (left) and antisymmetric (right) space-time precipitation spectra for TRMM (top), good models (middle) and poor models (bottom). Black asterisks indicate the $\alpha = 5\%$ statistically significant points from bootstrapping using a sample population involving all 25 Madden-Julian Oscillation Task Force (MJOTF) models. The equatorial wave dispersion relations using an equivalent depth of $h = 25$ m for background zonal winds of -3, 0, and 3 m/s are superimposed in the dotted, dashed, and solid gray lines, respectively.

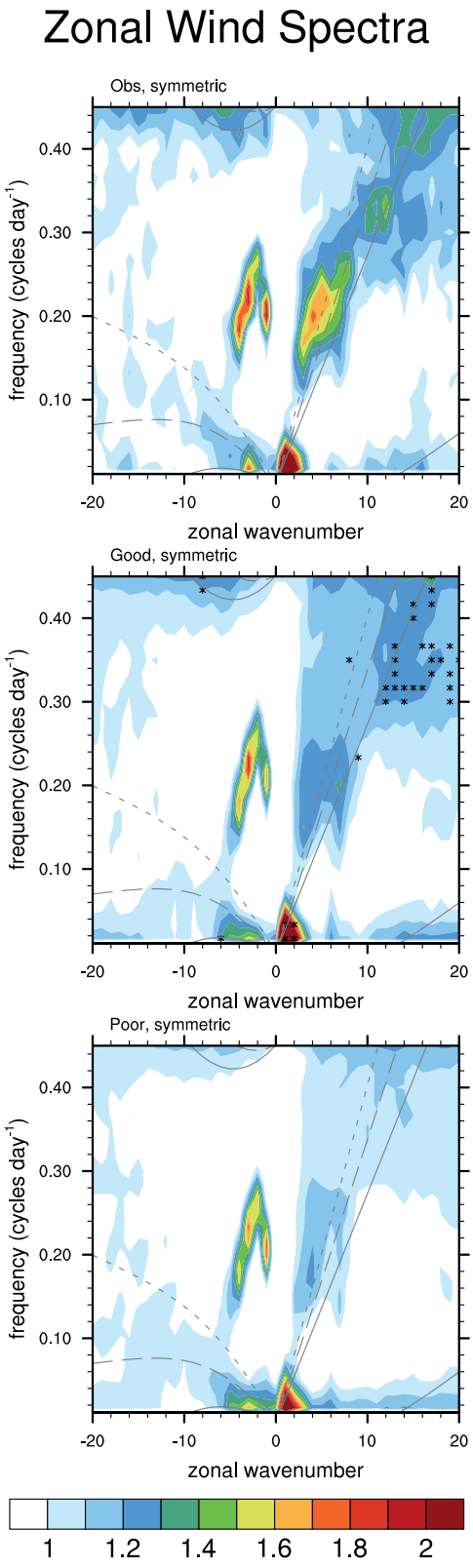

Figure 12. As in Figure 11, but for averaged 1000 to 850-hPa zonal wind symmetric spectra in ERA-Interim (top), good models (middle) and poor models (bottom).

are chosen, as used throughout this paper. For the observations (TRMM and ERA-Interim), only the vectors above a coherence-squared of 0.1 are shown.

Figure 13 shows that regions of high coherence-squared for Kelvin waves and the MJO (symmetric and antisymmetric) are both apparent in the observational data and good models while they are lacking in the poor models. Despite the good models having more accurate amplitudes of Kevin wave coherence-squared, their signal is shifted to higher frequencies, and even more so, higher wavenumbers. However, since there are few statistically significant points for Kelvin waves in the good models, it suggests that there are numerous MJOTF models that exhibit similar shifted behavior. The $n = 1$ ER wave coherence-squared does not show statistical significance (compared to all of the other models), which suggest model-wide biases in the zonal wind-precipitation coupling for ER waves. For the antisymmetirc MRG and $n = 0$ EIG coherence, both the good and poor models struggle to produce the observed coherence-squared between zonal wind and precipitation. At low frequencies in antisymmetric coherence, good models are relatively similar to TRMM and ERA-Interim while poor models have weak coherence. The phase vectors show how in-phase or out-of-phase the precipitation is with the zonal winds and are meaningful only when the coherence-squared is statistically significant. For TRMM and ERA-Interim, the MJO and Kelvin, MRG, and $n = 0$ EIG waves all have precipitation leading the zonal winds by about a 1/8–1/4 cycle while ER waves have the zonal winds in phase or leading precipitation by 1/8 cycle. For the good models, the MJO, Kelvin waves, and low frequency antisymmetric signals exhibit similar phasing as TRMM and ERA-Interim.

5. Summary and Conclusions

It is well-known that the MJO exerts significant influences on global weather and climate systems, however, the key processes that lead to the MJO's eastward propagation along the equator are poorly represented in current climate models (Ahn et al., 2017; Ahn, Kim, Kang, et al., 2020; Jiang et al., 2015). This study utilized output from 25 GCM simulations that participated in the MJO Task Force and GEWEX Atmospheric System Study GASS (MJOTF) program to identify the deficiencies in MJO dynamics in relation to MJO propagation.

The MJOTF model simulations were ranked based on their MJO propagation skill over the Indo-Pacific region via projections onto EOF2 of a new, precipitation-based intraseasonal index (S. Wang, 2020). Similar to other studies using the MJOTF models (Jiang et al., 2015; B. Wang & Lee, 2017), a good and poor MJO model group were identified based on MJO propagation skill across the Indo-Pacific. The eastward propagation of precipitation is simulated well in the good models while the poor models severely underestimate the eastward propagation, producing a stagnant or even slight westward propagation, in agreement with previous MJOTF studies (Jiang, 2017; Jiang et al., 2015; L. Wang et al., 2017; B. Wang & Lee, 2017).

Three dimensional precipitation amplitude independent regressions onto each model's precipitation-based intraseasonal index (PII) for unfiltered precipitation, zonal winds, horizontal divergence, apparent heating,

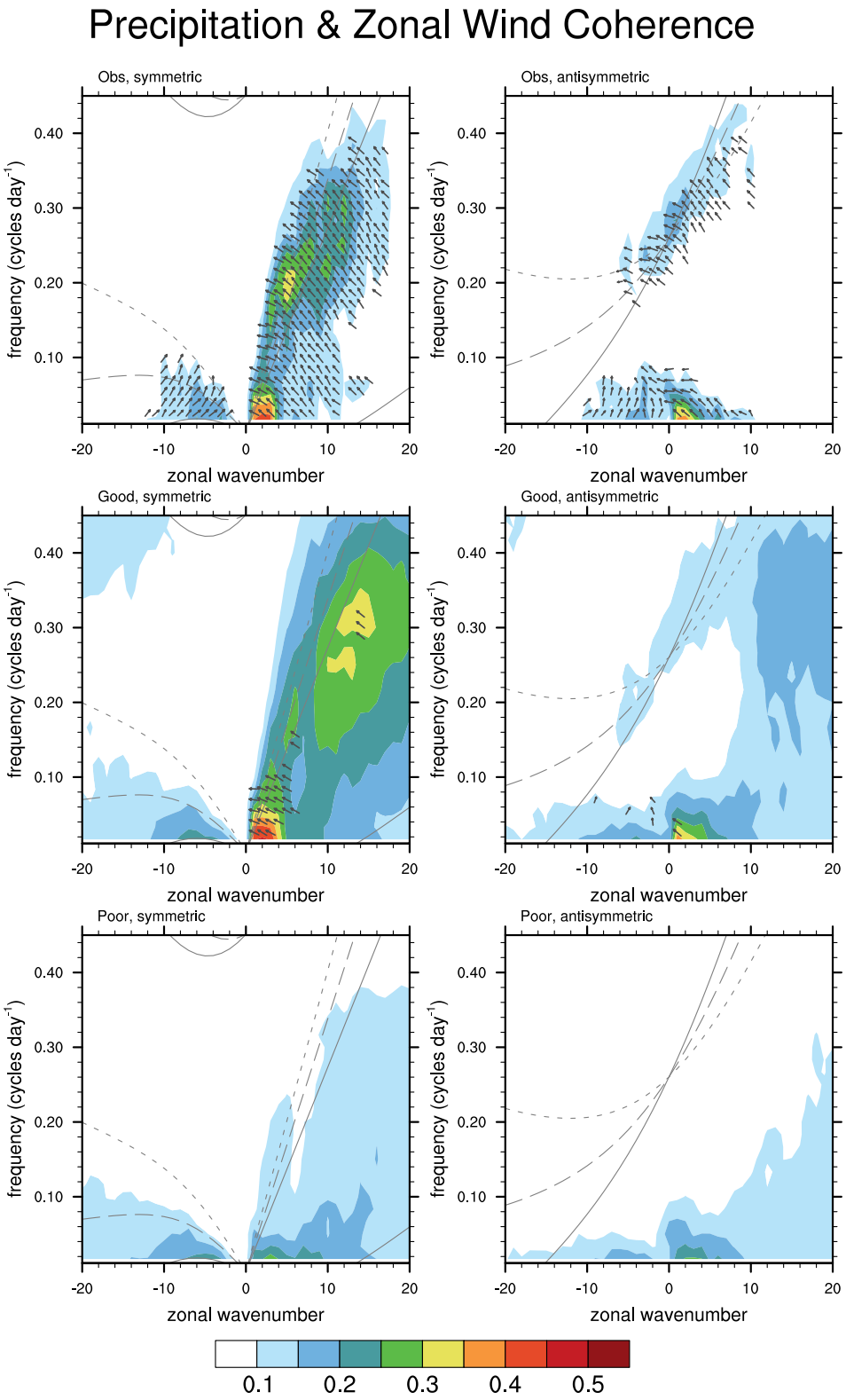

Figure 13. Coherence-squared (contours) and phase (vectors) between precipitation and averaged 1000 to 850-hPa zonal winds for the symmetric (left) and the antisymmetric spectra (right). Phase vectors are drawn only where the relationship is statistically significant at the $\alpha = 5\%$ level based on bootstrapping using a sample population involving all 25 Madden-Julian Oscillation Task Force (MJOTF) models. Upward-pointing arrows indicate the fields are in phase while an arrow pointing to the left indicates precipitation leads the zonal wind by a quarter cycle. The equatorial wave dispersion relations using an equivalent depth of $h = 25$ m for background zonal winds of −3, 0, and 3 m/s are superimposed in the dotted, dashed, and solid gray lines, respectively.

horizontal moisture advection, and vertical moisture advection were analyzed. Similar to other MJOTF studies, we find stark discrepancies between the good and poor models in large-scale equatorial Rossby (ER) and Kelvin wave circulations surrounding the MJO convective envelope. Good models tend to have a smaller ER wave response to the west than Kelvin wave response to the east at low and mid-levels, in line with ERA-Interim. Furthermore, the ER wave response to the dry anomaly ahead of the convectively active envelope is stronger in good models, further contributing their stronger dynamical response to the east. In contrast, poor models show a larger ER response to the west than Kelvin wave (plus ER wave) response to the east.

We quantify the role of large-scale asymmetries in the ER and Kelvin wave response for all of the models in a west/east (W/E) zonal wind speed ratio metric. The W/E ratio formulated here is similar to what has been used in recent studies to study how large-scale dynamics impact MJO propagation (e.g., B. Wang et al., 2018; L. Wang et al., 2018), with three main distinctions: (1) this W/E ratio is not computed over fixed regions west and east of convection, (2) this W/E ratio takes the vorticity associated with ER waves into account as it averages zonal wind speeds on both sides of the convection, and (3) this W/E ratio can be computed at upper levels. Our W/E ratio has very strong anticorrelations with MJO propagation skill above 0.8 in magnitude from 400 to 1000-hPa. Based on separately computed correlations between MJO propagation skill and west versus east zonal wind amplitude, the ER and Kelvin wave responses associated with the moist convective anomaly are most important below 750-hPa and from 450 to 750-hPa, respectively. Even though the W/E ratio itself has limited skill at upper levels, the good models and ERA-Interim tend to have larger zonal wind amplitudes on both sides of the convective envelope in the 150–250-hPa layer.

The poor models' anomalously strong ER wave response contributes to excessive low-level convergence (zonal and meridional components) and shallow diabatic heating co-located and to the west of the main convective envelope. In addition, there are weak divergence and convergence couplets ahead of the convective envelope and on its back side associated with a weaker dry anomaly and stratiform heating, respectively. Due to these biases, the poor models have little to no westward tilt with height of zonal winds, horizontal divergence, and apparent heating. We connect these divergence and diabatic heating biases to biases in both horizontal and vertical moisture advection. More specifically, poor models underestimate the magnitude of horizontal advection drying to the west and moistening to the east due to their weaker Kelvin and ER waves to the east and background specific humidity biases over the entire Indo-Pacific warm pool. In addition, vertical moisture advection produces more moistening in phase and to the west than the east in the poor models, especially below 650-hPa where anomalously large shallow moistening is co-located and to the west of the main convective center. We propose that the poor models precondition the low-level atmosphere to the west and just below the main convective center too heavily rather than to the east as in the good models and ERA-Interim which would explain their stagnant and even slight westward intraseasonal convection propagation.

Our conclusions support MJO propagation hypotheses involving both horizontal and vertical moisture and MSE advection (e.g., Ahn, Kim, Ham, & Park, 2020; Jiang, 2017; Sobel et al., 2014; L. Wang et al., 2017). At the same time, they reemphasize the need to improve our understanding of the moisture asymmetries in the boundary layer and the lower free troposphere, especially in relation the equatorial wave dynamics (e.g., Hsu & Li, 2012; B. Wang & Lee, 2017; L. Wang & Li, 2020b). Our results do not support the idea of the ER wave acceleration effect proposed by (L. Wang et al., 2018) as we find that models with stronger low- and mid-level ER waves to the west tend to have a lower MJO propagation skill. The reasons for this are not entirely clear but they may have to do with how we compute MJO propagation skill (using PII and/or excluding the base region, lags −2 to +2 days and 75°–85°E) and/or that we quantify ER and Kelvin waves via zonal wind speed anomaly rather than zonal wind anomaly west and east of MJO convection.

A wavenumber-frequency spectral analysis of precipitation and 850 to 1000-hPa averaged zonal wind further documented the contributions of equatorial waves to the coupling of large-scale dynamics and convection. TRMM precipitation and ERA-Interim zonal wind spectra both had large powers and coherence-squared for the MJO and Kelvin waves, with moderate $n = 1$ ER waves, and weak to moderate MRG, $n = 0$ EIG, and $n = 1$ IG waves. Similar precipitation and zonal wind spectra and coherence-squared and phase vectors were apparent in the good models except for the $n = 1$ ER wave zonal wind spectra, which were weaker and less concentrated in wavenumber. The poor models generally produced weaker wave modes compared to

good models except for $n = 1$ ER waves, which were similar in power and coherence-squared to the good models but even more spread out in wavenumber. While Kelvin wave precipitation and zonal wind spectra are better represented in the good models, they appear to be problematic in both model sets, with a common shift to higher wavenumbers and frequencies. Model-wide biases also exist in ER wave zonal wind spectra and coherence-squared, which is surprising considering their strong zonal wind amplitude correlations with MJO propagation skill (not shown). For the antisymmetric precipitation and zonal wind spectra, that is, MRG and $n = 0$ EIG waves, the good and poor models showed little to no signal compared to TRMM.

Based on the spectral analyses, there is evidence that the good models represent the MJO and Kelvin waves more in-line with observations but there are still substantial Kelvin and ER wave biases that may adversely affect the coupling of the dynamics and convection of equatorial wave modes in all MJOTF models. In relation to MJO propagation, we suggest that the zonal confinement and possibly meridional elongation of diabatic heating over the Indian Ocean of poor models may be related to their larger ER waves versus Kelvin wave circulation responses at low levels, as explored in MJO related studies (Schubert & Masarik, 2006; L. Wang et al., 2017) and idealized equatorial wave theory (Phlips & Gill, 1987). Another factor worth exploring for future work is how the differences in the horizontal distribution of boundary layer convergence may impact the ratio of ER waves to Kelvin waves at low levels. Lastly, future studies exploring spectral and cross-spectral analyses of more dynamical-convective variables would expand the knowledge of the relationship between equatorial waves and the MJO.

Data Availability Statement

The MJO Task Force/GASS climate model output along with ERA-Interim dynamic and thermodynamic fields and TRMM precipitation are located in the online repository: https://doi.org/10.25380/iastate.14555830. All scripts used to produce figures for this study are in the repository: https://iastate.box.com/v/mjotf-dynamics-2020.

Acknowledgments
The authors would like to thank George Kiladis and Juliana Dias for fruitful discussions on the spectral analyses of equatorial waves and for feedback of a previous form of the manuscript. The authors also would like to thank Shuguang Wang for providing the precipitation-based intraseasonal index (PII) and for advice on how to apply PII to the Madden-Julian Oscillation Task Force (MJOTF) output. Additionally, the authors acknowledge Brian Hornbuckle, Bill Gutowski, and two anonymous reviewers for their helpful feedback. Financial support comes from Iowa State University startup funding.

References

Adames, Á. F., & Wallace, J. M. (2015). Three-dimensional structure and evolution of the moisture field in the MJO. *Journal of the Atmospheric Sciences*, *72*(10), 3733–3754. https://doi.org/10.1175/JAS-D-15-0003.1

Ahn, M.-S., Kim, D., Ham, Y.-G., & Park, S. (2020). Role of maritime continent land convection on the mean state and MJO Propagation. *Journal of Climate*, *33*(5), 1659–1675. https://doi.org/10.1175/JCLI-D-19-0342.1

Ahn, M. S., Kim, D., Kang, D., Lee, J., Sperber, K. R., Gleckler, P. J., et al. (2020). MJO propagation across the maritime continent: Are CMIP6 models better than CMIP5 models? *Geophysical Research Letters*, *47*(11), e2020GL087250. https://doi.org/10.1029/2020GL087250

Ahn, M.-S., Kim, D., Kim, D., Sperber, K. R., Kang, I.-S., Maloney, E., et al. (2017). MJO simulation in CMIP5 climate models: MJO skill metrics and process-oriented diagnosis. *Climate Dynamics*, *49*, 4023–4045. https://doi.org/10.1007/s00382-017-3558-4

Bao, Q., Lin, P., Zhou, T., Liu, Y., Yu, Y., Wu, G., et al. (2013). The flexible global ocean-atmosphere-land system model, Spectral Version 2: FGOALS-s2. *Advances in Atmospheric Sciences*, *30*, 561–576. https://doi.org/10.1007/s00376-012-2113-9

Chen, G., & Wang, B. (2020). Circulation factors determining the propagation speed of the Madden-Julian oscillation. *Journal of Climate*, *33*(8), 3367–3380. https://doi.org/10.1175/JCLI-D-19-0661.1

Côté, J., Gravel, S., Méthot, A., Patoine, A., Roch, M., & Staniforth, A. (1998). The operational CMC-MRB global environmental multiscale (GEM) Model. Part I: Design considerations and formulation. *Monthly Weather Review*, *126*(6), 1373–1395. https://doi.org/10.1175/1520-0493(1998)126h1373:TOCMGEi2.0.CO;2

Dee, D. P., Uppala, S. M., Simmons, A. J., Berrisford, P., Poli, P., Kobayashi, S., et al. (2011). The ERA-Interim reanalysis: Configuration and performance of the data assimilation system. *Quarterly Journal of the Royal Meteorological Society*, *137*(656), 553–597. https://doi.org/10.1002/qj.828

Dias, J., & Kiladis, G. N. (2014). Influence of the basic state zonal flow on convectively coupled equatorial waves. *Geophysical Research Letters*, *41*(19), 6904–6913. https://doi.org/10.1002/2014GL061476

Fuchs-Stone, Ž., Raymond, D. J., & Sentić, S. (2019). A simple model of convectively coupled equatorial Rossby waves. *Journal of Advances in Modeling Earth Systems*, *11*(1), 173–184. https://doi.org/10.1029/2018MS001433

Gill, A. E. (1980). Some simple solutions for heat-induced tropical circulation. *Quarterly Journal of the Royal Meteorological Society*, *106*(449), 447–462. https://doi.org/10.1002/qj.49710644905

Gonzalez, A. O., & Jiang, X. (2017). Winter mean lower tropospheric moisture over the Maritime Continent as a climate model diagnostic metric for the propagation of the Madden-Julian oscillation. *Geophysical Research Letters*, *44*(5), 2588–2596. https://doi.org/10.1002/2016GL072430

Gonzalez, A. O., & Jiang, X. (2019). Distinct propagation characteristics of intraseasonal variability over the Tropical West Pacific. *Journal of Geophysical Research: Atmospheres*, *124*(10), 5332–5351. https://doi.org/10.1029/2018JD029884

Guo, Y., Waliser, D. E., & Jiang, X. (2015). A systematic relationship between the representations of convectively coupled equatorial wave activity and the Madden-Julian oscillation in climate model simulations. *Journal of Climate*, *28*(5), 1881–1904. https://doi.org/10.1175/JCLI-D-14-00485.1

Hagos, S., Zhang, C., Tao, W.-K., Lang, S., Takayabu, Y. N., Shige, S., et al. (2010). Estimates of tropical diabatic heating profiles: Commonalities and uncertainties. *Journal of Climate*, *23*(3), 542–558. https://doi.org/10.1175/2009JCLI3025.1

Hsu, P.-C., & Li, T. (2012). Role of the boundary layer moisture asymmetry in causing the eastward propagation of the Madden-Julian oscillation. *Journal of Climate*, *25*(14), 4914–4931. https://doi.org/10.1175/JCLI-D-11-00310.1

Huffman, G. J., Bolvin, D. T., Nelkin, E. J., Wolff, D. B., Adler, R. F., Gu, G., et al. (2007). The TRMM multisatellite precipitation analysis (TMPA): Quasi-global, multiyear, combined-sensor precipitation estimates at fine scales. *Journal of Hydrometeorology*, *8*(1), 38–55. https://doi.org/10.1175/JHM560.1

Hung, M.-P., Lin, J.-L., Wang, W., Kim, D., Shinoda, T., & Weaver, S. J. (2013). MJO and Convectively coupled equatorial waves simulated by CMIP5 climate models. *Journal of Climate*, *26*(17), 6185–6214. https://doi.org/10.1175/JCLI-D-12-00541.1

Jiang, X. (2017). Key processes for the eastward propagation of the Madden-Julian Oscillation based on multimodel simulations. *Journal of Geophysical Research: Atmospheres*, *122*(2), 755–770. https://doi.org/10.1002/2016JD025955

Jiang, X., Waliser, D. E., Xavier, P. K., Petch, J., Klingaman, N. P., Woolnough, S. J., et al. (2015). Vertical structure and physical processes of the Madden-Julian oscillation: Exploring key model physics in climate simulations. *Journal of Geophysical Research: Atmospheres*, *120*(10), 4718–4748. https://doi.org/10.1002/2014JD022375

Kikuchi, K., Kiladis, G. N., Dias, J., & Nasuno, T. (2018). Convectively coupled equatorial waves within the MJO during CINDY/DYNAMO: Slow Kelvin waves as building blocks. *Climate Dynamics*, *50*, 4211–4230. https://doi.org/10.1007/s00382-017-3869-5

Kikuchi, K., Wang, B., & Kajikawa, Y. (2012). Bimodal representation of the tropical intraseasonal oscillation. *Climate Dynamics*, *38*(9–10), 1989–2000. https://doi.org/10.1007/s00382-011-1159-1

Kiladis, G. N., Straub, K. H., & Haertel, P. T. (2005). Zonal and vertical structure of the Madden-Julian Oscillation. *Journal of the Atmospheric Sciences*, *62*(8), 2790–2809. https://doi.org/10.1175/JAS3520.1

Kim, D., Kug, J.-S., & Sobel, A. H. (2014). Propagating versus nonpropagating Madden-Julian oscillation events. *Journal of Climate*, *27*(1), 111–125. https://doi.org/10.1175/JCLI-D-13-00084.1

Kim, H., Vitart, F., & Waliser, D. E. (2018). Prediction of the Madden-Julian oscillation: A review. *Journal of Climate*, *31*(23), 9425–9443. https://doi.org/10.1175/JCLI-D-18-0210.1

Lappen, C.-L., & Schumacher, C. (2012). Heating in the tropical atmosphere: What level of detail is critical for accurate MJO simulations in GCMs? *Climate Dynamics*, *39*(9), 2547–2568. https://doi.org/10.1007/s00382-012-1327-y

Lin, J.-L., Kiladis, G. N., Mapes, B. E., Weickmann, K. M., Sperber, K. R., Lin, W., et al. (2006). Tropical intraseasonal variability in 14 IPCC AR4 climate models. Part I: convective signals. *Journal of Climate*, *19*(12), 2665–2690. https://doi.org/10.1175/JCLI3735.1

Liou, C. S., Chen, J. H., Terng, C. T., Wang, F. J., Fong, C. T., Rosmond, T. E., et al. (1997). The second-generation global forecast system at the Central Weather Bureau in Taiwan. *Weather and Forecasting*, *12*(3), 653–663. https://doi.org/10.1175/1520-0434(1997)012h0653:TSGGFSi2.0.CO;2

Madden, R. A., & Julian, P. R. (1971). Detection of a 40–50 day oscillation in the zonal wind in the Tropical Pacific. *Journal of the Atmospheric Sciences*, *28*(5), 702–708. https://doi.org/10.1175/1520-0469(1971)028⟨0702:DOADOI⟩2.0.CO;2

Madden, R. A., & Julian, P. R. (1972). Description of global-scale circulation cells in the Tropics with a 40–50 day period. *Journal of the Atmospheric Sciences*, *29*(6), 1109–1123. https://doi.org/10.1175/1520-0469(1972)029⟨1109:DOGSCC⟩2.0.CO;2

Maloney, E. D. (2009). The moist static energy budget of a composite tropical intraseasonal oscillation in a climate model. *Journal of Climate*, *22*(3), 711–729. https://doi.org/10.1175/2008JCLI2542.1

Matsuno, T. (1966). Quasi-geostrophic motions in the equatorial area. *Journal of the Meteorological Society of Japan*, *44*(1), 25–43. https://doi.org/10.2151/jmsj1965.44.125

Merryfield, W. J., Lee, W.-S., Boer, G. J., Kharin, V. V., Scinocca, J. F., Flato, G. M., et al. (2013). The canadian seasonal to interannual prediction system. Part I: Models and initialization. *Monthly Weather Review*, *141*(8), 2910–2945. https://doi.org/10.1175/MWR-D-12-00216.1

Molod, A., Takacs, L., Suarez, L. M., Bacmeister, J., Song, I.-S., & Eichmann, A. (2012). *The GEOS-5 atmospheric general circulation model: Mean climate and development from MERRA to Fortuna, NASA Technical Report Series on Global Modeling and Data Assimilation* (Tech. Rep. TM-2012-104606). Greenbelt, Maryland NASA: National Aeronautics and Space Administration.

Neale, R. B., Chen, C.-C., Gettelman, A., Lauritzen, P. H., Park, S., Williamson, D. L., & Taylor, M. A. (2012). *Description of the NCAR community atmosphere model (CAM 5.0)* (Tech. Rep. NCAR/TN-486+STR). Boulder, CO: National Center for Atmospheric Research.

Petch, J., Waliser, D., Jiang, X., Xavier, P., & Woolnough, S. (2011). A global model intercomparison of the physical processes associated with the Madden-Julian oscillation. *GEWEX News*, *21*, 3–5.

Phlips, P. J., & Gill, A. E. (1987). An analytic model of the heat-induced tropical circulation in the presence of a mean wind. *Quarterly Journal of the Royal Meteorological Society*, *113*(475), 213–236. https://doi.org/10.1002/qj.49711347513

Randall, D., Khairoutdinov, M., Arakawa, A., & Grabowski, W. (2003). Breaking the cloud parameterization deadlock. *Bulletin of the American Meteorological Society*, *84*(11), 1547–1564. https://doi.org/10.1175/BAMS-84-11-1547

Raymond, D. J., & Fuchs, Ž. (2009). Moisture modes and the Madden-Julian oscillation. *Journal of Climate*, *22*(11), 3031–3046. https://doi.org/10.1175/2008JCLI2739.1

Reynolds, R. W., Rayner, N. A., Smith, T. M., Stokes, D. C., & Wang, W. (2002). An improved in situ and satellite SST analysis for climate. *Journal of Climate*, *15*(13), 1609–1625. https://doi.org/10.1175/1520-0442(2002)015⟨1609:AIISAS⟩2.0.CO;2

Rui, H., & Wang, B. (1990). Development characteristics and dynamic structure of tropical intraseasonal convection anomalies. *Journal of the Atmospheric Sciences*, *47*(3), 357–379. https://doi.org/10.1175/1520-0469(1990)047⟨0357:DCADSO⟩2.0.CO;2

Saha, S., Moorthi, S., Wu, X., Wang, J., Nadiga, S., Tripp, P., et al. (2014). The NCEP climate forecast system Version 2. *Journal of Climate*, *27*(6), 2185–2208. https://doi.org/10.1175/JCLI-D-12-00823.1

Saha, S., Nadiga, S., Thiaw, C., Wang, J., Wang, W., Zhang, Q., et al. (2006). The NCEP climate forecast system. *Journal of Climate*, *19*(15), 3483–3517. https://doi.org/10.1175/JCLI3812.1

Schmidt, G. A., Kelley, M., Nazarenko, L., Ruedy, R., Russell, G. L., Aleinov, I., et al. (2014). Configuration and assessment of the GISS ModelE2 contributions to the CMIP5 archive. *Journal of Advances in Modeling Earth Systems*, *6*(1), 141–184. https://doi.org/10.1002/2013MS000265

Schubert, W. H., & Masarik, M. T. (2006). Potential vorticity aspects of the MJO. *Dynamics of Atmospheres and Oceans*, *42*, 127–151. https://doi.org/10.1016/j.dynatmoce.2006.02.003

Sobel, A., & Maloney, E. (2013). Moisture modes and the eastward propagation of the MJO. *Journal of the Atmospheric Sciences*, *70*(1), 187–192. https://doi.org/10.1175/JAS-D-12-0189.1

Sobel, A., Wang, S., & Kim, D. (2014). Moist static energy budget of the MJO during DYNAMO. *Journal of the Atmospheric Sciences*, *71*(11), 4276–4291. https://doi.org/10.1175/JAS-D-14-0052.1

Song, X., & Zhang, G. J. (2011). Microphysics parameterization for convective clouds in a global climate model: Description and single-column model tests. *Journal of Geophysical Research*, *116*(D2), D02201. https://doi.org/10.1029/2010JD014833

Stan, C., Khairoutdinov, M., DeMott, C. A., Krishnamurthy, V., Straus, D. M., Randall, D. A., et al. (2010). An ocean-atmosphere climate simulation with an embedded cloud resolving model. *Geophysical Research Letters*, *37*(1), L01702. https://doi.org/10.1029/2009GL040822

Stevens, B., Giorgetta, M., Esch, M., Mauritsen, T., Crueger, T., Rast, S., et al. (2013). Atmospheric component of the MPI-M Earth system model: ECHAM6. *Journal of Advances in Modeling Earth Systems*, *5*(2), 146–172. https://doi.org/10.1002/jame.20015

Tseng, W.-L., Tsuang, B.-J., Keenlyside, N. S., Hsu, H.-H., & Tu, C.-Y. (2015). Resolving the upper-ocean warm layer improves the simulation of the Madden-Julian oscillation. *Climate Dynamics*, *44*, 1487–1503. https://doi.org/10.1007/s00382-014-2315-1

Voldoire, A., Sanchez-Gomez, E., Salas y Mélia, D., Decharme, B., Cassou, C., Sénési, S., et al. (2013). The CNRM-CM5.1 global climate model: Description and basic evaluation. *Climate Dynamics*, *40*, 2091–2121. Retrieved from: https://hal.archives-ouvertes.fr/hal-00833024

Wang, B., & Chen, G. (2016). A general theoretical framework for understanding essential dynamics of Madden-Julian oscillation. *Climate Dynamics*, *49*, 2309–2328. https://doi.org/10.1007/s00382-016-3448-1

Wang, B., & Lee, S.-S. (2017). MJO Propagation shaped by zonal asymmetric structures: Results from 24 GCM simulations. *Journal of Climate*, *30*(19), 7933–7952. https://doi.org/10.1175/JCLI-D-16-0873.1

Wang, B., Lee, S.-S., Waliser, D. E., Zhang, C., Sobel, A., Maloney, E., et al. (2018). Dynamics-oriented diagnostics for the Madden-Julian Oscillation. *Journal of Climate*, *31*(8), 3117–3135. https://doi.org/10.1175/JCLI-D-17-0332.1

Wang, B., Liu, F., & Chen, G. (2016). A trio-interaction theory for Madden-Julian oscillation. *Geoscience Letters*, *3*, 34. https://doi.org/10.1186/s40562-016-0066-z

Wang, L., & Li, T. (2020a). Effect of vertical moist static energy advection on MJO eastward propagation: Sensitivity to analysis domain. *Climate Dynamics*, *54*, 2029–2039. https://doi.org/10.1007/s00382-019-05101-8

Wang, L., & Li, T. (2020b). Reexamining the MJO moisture mode theories with normalized phase evolutions. *Journal of Climate*, *33*(19), 8523–8536. https://doi.org/10.1175/JCLI-D-20-0202.1

Wang, L., Li, T., Maloney, E., & Wang, B. (2017). Fundamental causes of propagating and nonpropagating MJOs in MJOTF/GASS models. *Journal of Climate*, *30*(10), 3743–3769. https://doi.org/10.1175/JCLI-D-16-0765.1

Wang, L., Li, T., & Nasuno, T. (2018). Impact of Rossby and Kelvin wave components on MJO eastward propagation. *Journal of Climate*, *31*(17), 6913–6931. https://doi.org/10.1175/JCLI-D-17-0749.1

Wang, S. (2020). A precipitation-based index for tropical intraseasonal oscillations. *Journal of Climate*, *33*(3), 805–823. https://doi.org/10.1175/JCLI-D-19-0019.1

Watanabe, M., Suzuki, T., O'ishi, R., Komuro, Y., Watanabe, S., Emori, S., et al. (2010). Improved climate simulation by MIROC5: Mean states, variability, and climate sensitivity. *Journal of Climate*, *23*(23), 6312–6335. https://doi.org/10.1175/2010JCLI3679.1

Wheeler, M., & Kiladis, G. N. (1999). Convectively coupled equatorial waves: Analysis of clouds and temperature in the wavenumber-frequency domain. *Journal of the Atmospheric Sciences*, *56*(3), 374–399. https://doi.org/10.1175/1520-0469(1999)056⟨0374:CCEWAO⟩2.0.CO;2

Wu, T., Yu, R., Zhang, F., Wang, Z., Dong, M., Wang, L., et al. (2010). The Beijing Climate Center atmospheric general circulation model: Description and its performance for the present-day climate. *Climate Dynamics*, *34*(1), 123–147. https://doi.org/10.1007/s00382-008-0487-2

Wu, X., & Deng, L. (2013). Comparison of moist static energy and budget between the GCM-simulated Madden-Julian oscillation and observations over the Indian Ocean and Western Pacific. *Journal of Climate*, *26*(14), 4981–4993. https://doi.org/10.1175/JCLI-D-12-00607.1

Yanai, M., Esbensen, S., & Chu, J.-H. (1973). Determination of bulk properties of tropical cloud clusters from large-scale heat and moisture budgets. *Journal of the Atmospheric Sciences*, *30*(4), 611–627. https://doi.org/10.1175/1520-0469(1973)030⟨0611:DOBPOT⟩2.0.CO;2

Yu, J.-Y., & Neelin, J. D. (1994). Modes of tropical variability under convective adjustment and the Madden-Julian oscillation. Part II: Numerical results. *Journal of the Atmospheric Sciences*, *51*(13), 1895–1914. https://doi.org/10.1175/1520-0469(1994)051⟨1895:MOTVUC⟩2.0.CO;2

Yukimoto, S., Adachi, Y., Hosaka, M., Sakami, T., Yoshimura, H., Hirabara, M., et al. (2012). A new global climate model of the Meteorological Research Institute: MRI-CGCM3 - Model description and basic performance. *Journal of the Meteorological Society of Japan*, *90A*, 23–64. https://doi.org/10.2151/jmsj.2012-A02

Zhang, C. (2005). Madden-Julian oscillation. *Reviews of Geophysics*, *43*(2). https://doi.org/10.1029/2004RG000158

Zhang, C. (2013). Madden-Julian oscillation: Bridging weather and climate. *Bulletin of the American Meteorological Society*, *94*(12), 1849–1870. https://doi.org/10.1175/BAMS-D-12-00026.1

Zhang, C., Adames, Á. F., Khouider, B., Wang, B., & Yang, D. (2020). Four theories of the Madden-Julian oscillation. *Reviews of Geophysics*, *58*(3), e2019RG000685. https://doi.org/10.1029/2019RG000685

Zhang, G. J., & Mu, M. (2005). Simulation of the Madden-Julian oscillation in the NCAR CCM3 using a revised Zhang-McFarlane convection parameterization scheme. *Journal of Climate*, *18*(19), 4046–4064. https://doi.org/10.1175/JCLI3508.1

Zhu, H., Hendon, H., Dix, M., Sun, Z., Dietachmayer, G., & Puri, K. (2013). Vertical structure and diabatic processes of the MJO, A global model inter-comparison Project: Preliminary results from ACCESS model. *CAWCR Research Letters*, *10*, 2034–2038.